

**Autocorrelation functions and  
Doppler spectra measured by the  
TIGER SuperDARN radar**

**A thesis presented by**

**Kevin Hannah**

**In partial fulfilment  
of the requirements for the degree**

**Bachelor of Space Science (Honours)**

**In the subject of**

**Physics**

**Department of Physics  
School of Engineering and Mathematical  
Sciences**

**La Trobe University  
Bundoora, Melbourne  
Australia**

**November, 2004**

# TABLE OF CONTENTS

<b>ABSTRACT</b> .....	<b>4</b>
<b>STATEMENT OF AUTHORSHIP</b> .....	<b>5</b>
<b>ACKNOWLEDGEMENTS</b> .....	<b>6</b>
<b>CHAPTER 1: THE IONOSPHERE</b> .....	<b>7</b>
<b>1.1 GEOSPACE</b> .....	7
<b>1.2 THE NEUTRAL ATMOSPHERE</b> .....	8
<b>1.3 THE IONOSPHERE</b> .....	10
<b>1.4 IONOSPHERIC IRREGULARITIES AND THEIR CREATION</b> .....	13
<i>1.4.1 Plasma instabilities</i> .....	14
<b>1.4.1.1 Gradient drift instability</b> .....	15
<b>1.4.1.2 Two-stream instability</b> .....	15
<i>1.4.2 Large- and small-scale structures</i> .....	16
<b>1.5 OPEN-CLOSED MAGNETIC FIELD LINE BOUNDARY</b> .....	16
<b>1.6 THEORY OF COLLECTIVE WAVE SCATTERING</b> .....	17
<i>1.6.1 Scattering in the limit of long correlation length fluid turbulence</i> .....	19
<i>1.6.2 Scattering in the limit of short correlation length</i> .....	19
<i>1.6.3 Intermediate case</i> .....	20
<b>CHAPTER 2: THE INSTRUMENTATION</b> .....	<b>22</b>
<b>2.1 SUPERDARN</b> .....	22
<b>2.2 TIGER AND HALLEY SUPERDARN RADARS</b> .....	23
<i>2.2.1 The Tasman International Geospace Environment Radar (TIGER)</i> .....	23
<i>2.2.2 The Halley SuperDARN radar</i> .....	26
<b>2.3 PULSE SET TECHNIQUE AND DATA ANALYSIS</b> .....	27
<i>2.3.1 Autocorrelation (ACFs) and “FITACF”</i> .....	27
<i>2.3.2 Summary plots</i> .....	31
<i>2.3.3 TGRaw</i> .....	32
<b>2.4 MULTI-PEAKED SPECTRA</b> .....	32
<b>CHAPTER 3: MOVEMENT OF THE DEEP POLAR IONOSPHERE</b> .....	<b>35</b>

3.1 ANTISUNWARD DRIFT DUE TO MAGNETIC RECONNECTION .....	35
3.2 EXPERIMENTAL DESIGN AND DATA SELECTION .....	37
3.3 HALLEY AND TIGER OBSERVATIONS OF ANTISUNWARD DRIFT .....	38
3.4 HALLEY AND TIGER OBSERVATIONS OF THE DEEP POLAR IONOSPHERE .....	40
<b>CHAPTER 4 – SPECTRAL WIDTHS, LORENTZIAN OR</b>	
<b>GAUSSIAN? .....</b>	<b>43</b>
4.1 WHY USE LORENTZIAN OR GAUSSIAN CURVES? .....	43
4.2 LORENTZIAN VERSUS GAUSSIAN SPECTRAL WIDTHS .....	43
4.3 PHASE TRANSITION IN THE HIGH-LATITUDE F-REGION PLASMA .....	48
<b>CHAPTER 5 – MULTI-PEAKED DOPPLER SPECTRA .....</b>	<b>50</b>
5.1 IDENTIFICATION OF MULTI-PEAKED DOPPLER SPECTRA .....	50
5.2 DOPPLER CHARACTERISTICS OBSERVED USING THE BURG ANALYSIS .....	52
5.3 OCCURRENCE OF MULTI-PEAKED SPECTRA .....	53
<b>SUMMARY AND CONCLUSIONS .....</b>	<b>56</b>
<b>REFERENCES .....</b>	<b>58</b>

## Abstract

SuperDARN HF backscatter radars have previously been used to study various phenomena in the auroral and polar cap ionosphere. As the TIGER SuperDARN radar is presently the lowest latitude radar in the network, it is particularly suited for studying the transition in plasma characteristics across the nightside open–closed magnetic field line boundary. Previous studies have shown the spectral width boundary coincides with the open-closed magnetic field line boundary in the pre-midnight sector. The new analysis of TIGER data presented here has revealed, for the first time, spatial organisation in the distribution of Gaussian and Lorentzian Doppler spectra. This study showed that Gaussian Doppler spectra were associated with regions of low spectral width, and Lorentzian Doppler spectra were associated with regions of high spectral width. Therefore, the Gaussian and Lorentzian Doppler spectra were concentrated on closed and open magnetic field lines, respectively. The distinct changes in line-of-sight Doppler velocity, spectral width, and correlation times and lengths across this boundary imply the occurrence of a phase transition in the plasma characteristics. A new form of data analysis known as a Burg analysis (a maximum entropy method) was applied to the autocorrelation functions to locate multi-peaked spectra where previously only single-peaked spectra had been observed. This new method improved the Doppler resolution as compared to the standard approach and subsequently resolved multiple peaks in many high spectral width spectra. This implies the existence of small-scale vortices and confirms the turbulent character of the high spectral width region. Lastly, with the concurrent use of the Halley radar, antisunward drift and the decay of spectral widths was observed across the deep polar cap ionosphere, a rarely studied region.

## Statement of Authorship

Except where reference is made in the text of the thesis, this thesis contains no material published elsewhere or extracted in whole or in part from a thesis submitted for the award of any another degree or diploma.

No other person's work has been used without due acknowledgement in the main text of the thesis.

The thesis has not been submitted for the award of any degree or diploma in any other tertiary institution.

---

Kevin Hannah

## Acknowledgements

Firstly I would like to thank Dr Murray Parkinson for all of his advice, insight and understanding of all theories concerning this thesis, and the willingness to explain them, no matter how trivial. Your assistance throughout this thesis has been immeasurable.

I would like to thank Professor Peter Dyson for his wisdom and support throughout this year. Thank you for allowing this opportunity to complete my thesis.

Thank you to Professor A. V. Koustov and Dr. D. Danskin for allowing the use of their Burg analysis code. Also thank you to Dr C. Waters for your assistance with all things concerning TGRaw.

Many thanks to my fellow honour students who showed profound wisdom when it was least expected.

I would like to thank my Father for his continuous support and encouragement. And finally my Mother, without whom, I would never have aspired to reach this point.

# Chapter 1: The Ionosphere

## 1.1 Geospace

The ionosphere and upper atmosphere are strongly affected by the dynamics of the near-Earth space environment known as geospace. Looking at the Earth's geomagnetic field, to first approximation it can be represented as a dipole. After about 10 Earth radii, direct interaction of the field with the solar wind occurs, and this ultimately affects the Earth in many ways. The Sun does not just radiate electromagnetic waves which interact with the Earth's atmosphere, but its atmosphere also slowly bleeds away into space to form the solar wind (Scolvi, 1970). This solar wind contains an outflow of hydrogen protons and  $\alpha$ -particles ejected from the solar corona. The interaction between the Sun and the Earth is dependant on a weak magnetic field know as the interplanetary magnetic field (IMF). The IMF is an extension of the Sun's magnetic field, and is frozen into the solar wind plasma. The solar wind flows radially out from the Sun, but because of its rotation, the magnetic field takes the form of an Archimedean spiral. The solar wind has an average speed of around  $400 \text{ km s}^{-1}$ , and can exceed speeds of  $1200 \text{ km s}^{-1}$  during "fast flows" associated with coronal mass ejections (CMEs) (CALSPACE). Upon encountering the Earth, a bow shock is formed at about 12-13 Earth radii.

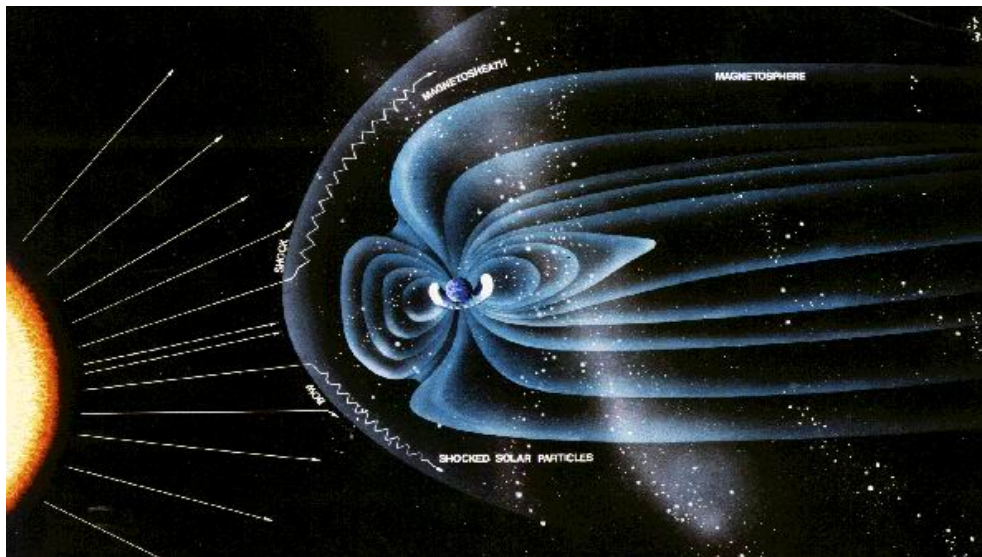


**Figure 1.0:** The solar wind emanating from the Sun compresses the sunward side of the magnetosphere and extends the magnetotail (CALSPACE).

This is the point at which the solar wind becomes sub-sonic due to the force of the Earth's magnetosphere pushing back. Between the bow shock and magnetopause is the magnetosheath, a region where the solar wind becomes turbulent (Hargreaves, 1992). The magnetopause is the boundary to the magnetosphere which contains the Earth's magnetic field. The solar wind compresses the magnetic field on the sunward side and pushes the magnetotail millions of kilometres back from the Earth (CALSPACE, ; Spaceweb, 1998; Balthazor, 2000; Hunsucker and Hargreaves, 2002). This can be seen in Figure 1.0. Note that field lines at low latitude form closed loops between the Northern and Southern Hemispheres, whilst at high latitudes the field lines are swept back from the Earth in an anti-sunward direction. There is a boundary in the magnetosphere between the open and closed magnetic field lines. Reconnection between open and closed field lines communicate electrical potential from the solar wind to the high-latitude ionosphere (Hunsucker and Hargreaves, 2002). The resulting electric fields drive plasma motion in the ionosphere. Open field lines connect to the IMF and permit magnetosheath particles to travel down into the Earth's ionosphere causing field-aligned currents and the dayside aurora. The energetic electrons and protons responsible for the nightside aurora are accelerated on the stretched magnetic field lines located just Earthward of the boundary between open and closed field lines in the magnetotail (Balthazor, 2000).

## 1.2 The Neutral Atmosphere

The atmospheric structure is governed by four properties: *pressure* ( $P$ ), *temperature* ( $T$ ), *density* ( $\rho$ ), and *composition*. These variables are not all independent of one another and hence sometimes only some are needed to define a region. The main structure of the atmosphere is determined by the variation of temperature with height (Hargreaves, 1992). This gives rise to a number of 'spheres' as the atmosphere is spherically stratified. Each of these 'spheres' represents a defined set of values for the four properties above. There are two basic 'spheres' which divide the atmosphere. These are the *homosphere* and the *heterosphere*.

The homosphere is the region below about 100 km where the composition of the atmosphere is relatively constant, with some minor components standing out at certain altitudes. In this region there are three basic sub 'spheres', namely the troposphere, stratosphere, and mesosphere. The lowest region, the troposphere, has a temperature profile which decreases with height (Hargreaves, 1992; Hunsucker and Hargreaves, 2002). The heating in this region is due to re-radiation from the Earth. Next there is the stratosphere which actually has increasing temperature with height. This is due to absorption of ultra-violet radiation by ozone. Finally the temperature in the mesosphere decreases with height, and reaches the lowest temperature found in the atmosphere at around 180 K.

Above the homosphere is the heterosphere. This is a region where the various components in the atmosphere separate due to gravity and the composition is no longer well mixed, and hence it becomes heterogeneous. This region contains the thermosphere where UV radiation keeps the temperature gradient constantly positive (Hunsucker and Hargreaves, 2002). Eventually the temperature in the thermosphere reaches its peak of around 1300 K and remains constant, as seen in Figure 1.1.

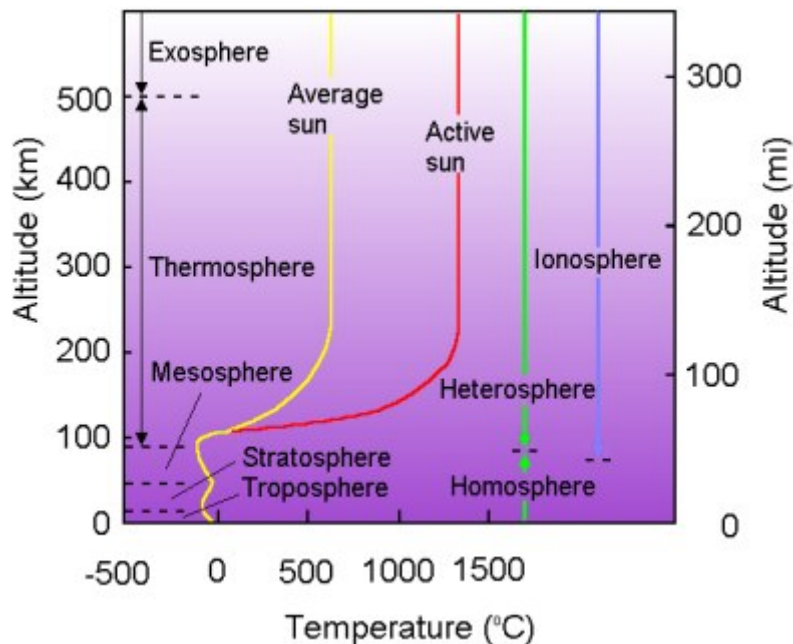
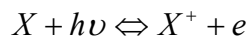


**Figure 1.1:** Temperature profile of the upper atmosphere (Hackworth, 2004).

There is also a region known as the ionosphere. This region can be probed by HF radar, as was the case in this study.

### 1.3 The Ionosphere

The ionosphere is a region of the atmosphere between about 60 and 1000 km in altitude where X-ray and ultra violet radiation from the Sun has ionised the atmosphere to form a strongly magnetised plasma (Rishbeth and Garriot, 1969; Hunsucker and Hargreaves, 2002). The ionisation process follows the general form,



where  $X$  is an atom or molecule,  $h\nu$  is a packet of energy photon, and  $e$  is an electron. Although polarisation fields can form within the ionosphere, overall the plasma is electrically neutral. The collision frequency between ions and neutral atoms decreases exponentially with height (Hargreaves, 1992), and the recombination times become large for the plasma in the upper ionosphere. The ionosphere is an important region for communications and experimental physics because of its ability to refract high frequency (HF: 3 to 30 MHz) radio waves.

In the ionosphere, the height profile is governed by the variation in the electron density. A vertical profile of the ionosphere shows four distinct layers, as seen in Figure 1.2. These layers are the D, E, F1 and F2 layers and are defined by their height, composition, dynamics, and electron densities. This can be seen in Table 1.0.

**Table 1.0:** Properties of the daytime ionospheric layers (Hargreaves, 1992).

Region	Height	Composition	Electron Density
D	60 – 90 km	NO <sup>+</sup> , O <sub>2</sub> <sup>+</sup> , Negative ions	10 <sup>8</sup> – 10 <sup>10</sup> m <sup>-3</sup>
E	90 – 160 km	NO <sup>+</sup> , O <sub>2</sub> <sup>+</sup>	around 10 <sup>11</sup> m <sup>-3</sup>
F1	160 – 210 km	O <sup>+</sup> , N <sub>2</sub> <sup>+</sup> , NO <sup>+</sup> , O <sub>2</sub> <sup>+</sup>	10 <sup>11</sup> – 10 <sup>12</sup> m <sup>-3</sup>
F2	210 – 450 km	O <sup>+</sup> , O <sub>2</sub> <sup>+</sup> , H <sup>+</sup> , He <sup>+</sup>	around 10 <sup>12</sup> m <sup>-3</sup>

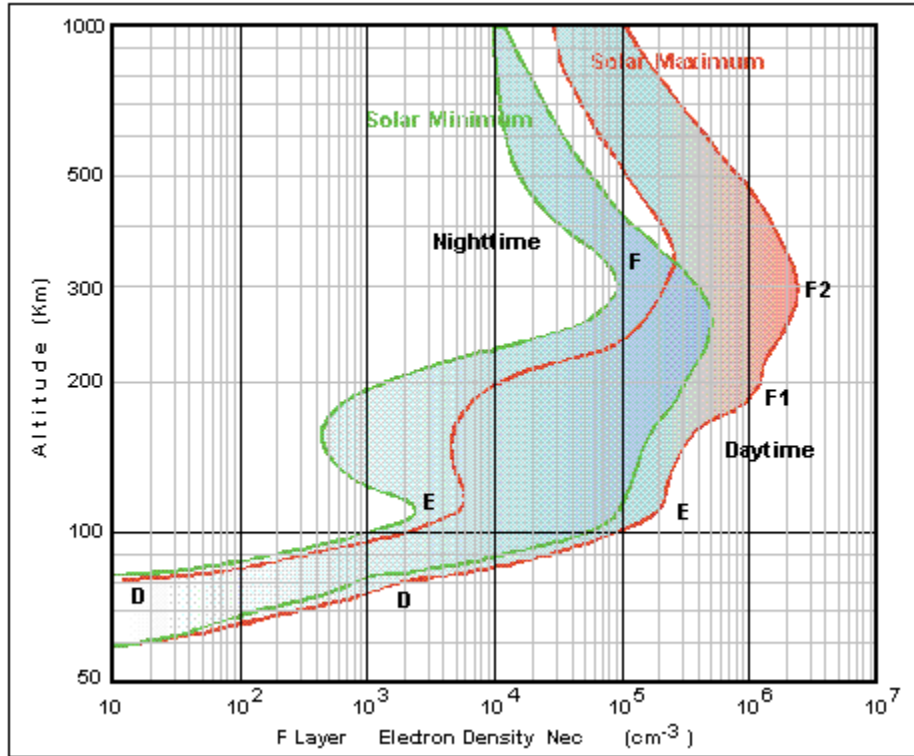
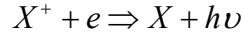


**Figure 1.2:** Day and night vertical profiles of electron density where the green lines are for solar minimum and the red lines are for solar maximum (Balthazor, 2000).

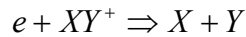
The first layer, the D-region, is a very turbulent region with relatively high pressure, and it is caused by a varying array of sources (Hargreaves, 1992). The Lyman- $\alpha$  line ionises nitric oxide (NO), and there is a small contribution due to EUV. Solar X-rays vary as a major and minor participant in the ionisation of this region. At high latitudes, precipitating particles with relativistic energies can also affect ionisation in this region. Cosmic rays produce ionisation in proportion to the air density and they are a continuous source of ionisation during the day and night (Hargreaves, 1992). They can become a major source of ionisation. However, the D-region is generally much weaker at night.

The D-region is detectable using rocket-based wave propagation techniques. It is the principle region where radio absorption occurs, and it can become a large problem when trying to sound the upper ionosphere with HF radar, especially during the day time or during magnetic storms.

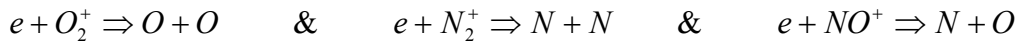
The next layer is the E-region. Here, molecular oxygen absorbs EUV in the 80–102 nm range to form  $O_2^+$ , while X-rays of scale 1–10 nm ionise all constituents, namely forming  $N_2^+$ ,  $O_2^+$  and  $O^+$ , but most abundant are the  $NO^+$  ions (Hargreaves, 1992). In the E-region, there are two types of recombination for the plasma, *radiative* and *dissociative*. Radiative recombination is basically the ionisation process in reverse. This process is very infrequent and has little effect on recombination.



Dissociative recombination is up to  $10^5$  times faster and the loss of ions and electrons is due to molecular ions.



The main reactions in the E-region are then



Although plasma density in the E-region is controlled by the solar zenith angle, it does not totally vanish at night and remains with a lower electron density (Figure 1.2). One of the contributions to the nightside ionisation is the injection of long-lived metallic ions by meteors which occur in the E-region (Mathews et al., 2002).

There exists a transient, thin, and sometimes intense layer of ionisation that occurs in the E layer known as *sporadic E*. These layers can be less than 1 kilometre thick (in height), and yet extend over hundreds of kilometres horizontally. At mid latitudes, sporadic-E is most likely due to wind shear (Whitehead, 1971). At high latitudes, in the region of aurora, thicker sporadic layers form due to the production of ionisation by precipitating particles with energies 1–10 keV. Sporadic E layers drift with speeds of  $\sim 10\text{--}200 \text{ m s}^{-1}$ . Sporadic E is important because its plasma frequency is often higher than the E-layer, and it reflects signals that would otherwise propagate to a much greater altitude and thus ground range.

The third layer is the F1 region. This region is much like the E-region in that it follows much of the same process for ionisation and recombination. In the F1-region, ionisation is mostly due to radiation in the 20–90 nm range which is absorbed by atomic oxygen (Hargreaves, 1979). As the primary ion is now  $O^+$ , not a molecular ion, the ion must

undergo a charge re-distribution so that dissociative recombination can occur similar to that in the E-region. Charge re-distribution is of the form



In the case of the F1 region, the characteristic reactions are found to be



These reactions can then be followed by dissociative recombination. Looking at Figure 1.1, it is interesting to note that the F1 peak is more of a ledge than a peak, and that the layer can seem to disappear completely.

The final region is the F2 region, and in some ways it is the most interesting region of all. Although the photochemistry of this region is similar to those of the lower layers, it is a less predictable region because of dynamic transport processes acting on the ionised and neutral components. For example, F2 region ionisation can escape to the plasmasphere during the daytime. Conversely, particles can re-enter the F2 region from the plasmasphere during the nighttime. Hence the mid-latitude ionosphere does not necessarily disappear at night, but can persist in a relatively substantial form. An explanation of all the dynamic processes controlling space weather within the F2 region is beyond the scope of this thesis. Although ionospheric modellers have made good progress in reproducing the variability observed during quiet times and magnetic storms, there are still many problems to solve.

## **1.4 Ionospheric irregularities and their creation**

Irregularities are a common feature in the F-region ionosphere. They have scale sizes ranging from the ion gyroradius of approximately 10 m (at low altitudes) to large-scale structures of 1000 km and beyond (Hargreaves, 1992; Hunsucker and Hargreaves, 2002). Although the instrument used in this study is an HF radar which looks primarily at decametre scale irregularities, a description of large scale irregularities is necessary because small-scale structures are thought to form via a cascade of energy from larger

scale structures. In the following sections, we look at the instabilities which create ionospheric irregularities.

### 1.4.1 Plasma instabilities

When looking at a plasma, such as the strongly magnetised plasma of the ionosphere, it is generally assumed it is in a state of equilibrium. This simplifies the theory. When looking at the ionosphere, instabilities appear in the plasma that occur because the ionosphere is not always in perfect equilibrium, and there is free energy which can create self-excited waves (Chen, 1984). These instabilities attempt to bring the system closer to equilibrium by using the available free energy. According to Chen (1984) there are four main categories of instabilities:

1. Streaming instabilities. These are due to different species having different drifts compared to one another because of a current being driven through the plasma or because a beam of energetic particles travels through the plasma. This drift energy can excite waves that oscillate so as to reduce the drift energy toward an unperturbed state.
2. Rayleigh-Taylor instabilities. At certain places in the plasma, a large density gradient can form so that overall the plasma is no longer uniform. These gradients are 'seeded' by an external force which drives the instability. This instability can be thought of in terms of a heavy fluid sitting on top of a less dense fluid. The heavy fluid tries to sink and the less dense fluid rises through the more dense fluid, thereby forming bubbles.
3. Universal instabilities. This instability arises when a plasma is confined and there are no forces (electric or gravitational) to drive the plasma, yet the plasma is not in thermodynamic equilibrium. The plasma will try to expand due to its internal pressure which can drive an instability. This instability will be present in finite regions of plasma.

4. Kinetic instabilities. The plasma is assumed to have a Maxwellian velocity distribution so as to be in thermodynamic equilibrium, but this is not always true. If the velocity distribution has a non-Maxwellian component then the anisotropy of the distribution can lead to an instability.

There are many different instabilities that fit into each of these categories. When looking at the mid- to high-latitude E and F region ionosphere, the main irregularities that are observed are due to the gradient drift instability (Rayleigh-Taylor type) and the two-stream instability (streaming type). These two instabilities will need to be explained further.

#### **1.4.1.1 Gradient drift instability**

The gradient drift instability is also commonly known as the  $\mathbf{E} \times \mathbf{B}$  instability, a kind of interchange instability (Spaceweb, 1998). If a slight enhancement of the plasma density is present, and an external force such as that due to an electric field, gravity, or neutral air winds, then a charge separation can take place. This charge separation produces a small polarization electric field which increases the disturbance, thus producing irregularities. This instability is a common mechanism by which irregular structures in the F-region breaks down to smaller ones (Hargreaves, 1992). The formation of this instability in the E-region requires an electric field in the plasma parallel to the plasma density gradient. In the F-region, the electric field must be perpendicular to the plasma density gradient.

#### **1.4.1.2 Two-stream instability**

If electrons and ions differ in velocity by more than the ion-acoustic speed an instability is generated called the two-stream instability. The waves produced by this instability propagate nearly perpendicular to the magnetic field. This instability grows more rapidly at shorter wavelengths. The importance of this instability is greatest in the E-region at

low and high latitudes (Hargreaves, 1992). At altitudes of ~85 km and more the electrons are magnetized and exhibit Hall drift perpendicular to the electric field, whilst the ions are unmagnetized and exhibit Pedersen drift parallel to the electric field. Therefore, the electrons stream through the ions, exciting the instability. In the F-region, the ions and electrons both drift with the Hall velocity, so their relative drift speed is essentially zero, and the instability is inoperative. In the D-region, the electrons and ions both move with the neutral wind velocity. Hence this instability is most likely to occur in the E-region dynamo.

### **1.4.2 Large- and small-scale structures**

The gradient drift instability is thought to be crucial to the creation of irregularities in both the E and F-regions of the high-latitude ionosphere. Patches and blobs, the two main large-scale structures in the high latitude ionosphere, are both thought to support the gradient drift instability. These irregularities are primarily observed antisunward of the polar cusp, and are clearly defined during the winter (Hargreaves, 1992; Hunsucker and Hargreaves, 2002). Small-scale decametre structures in the F-region are thought to be caused by secondary gradient drift instabilities acting upon the larger-scale structures. Whilst the gradient drift instability still causes many of the irregularities in the E-region, the two-stream instability is also a dominant cause of irregularities in this region.

### **1.5 Open-closed magnetic field line boundary**

The open-closed magnetic field line boundary is the boundary between the closed field lines joining the northern and southern hemispheres and the open field lines which connect to the interplanetary magnetic field (IMF). It is the boundary that separates the plasma that is constrained by the Earth's magnetic field from that which travels along field lines which connect to the Sun's magnetic field (Spaceweb, 1998). This boundary is ever shifting due of solar wind variability and magnetic substorms. The dayside position

of this boundary is known to depend on the IMF and solar wind conditions. The night side position is sensitive to the solar wind and IMF conditions, but it is also sensitive to magnetic substorm and storm activity. The transition from low spectral widths to high spectral widths, as seen with SuperDARN radars, is known to coincide with the open closed field line boundary when looking at the dayside under IMF southward conditions (Chisham et al., 2003), and the nightside ionosphere in the pre-midnight sector (Parkinson et al., 2002).

## 1.6 Theory of collective wave scattering

The theory of collective wave scattering in a non-uniform plasma implies that the Doppler spectrum will display a Lorentzian shape for velocity fluctuations with correlation lengths shorter than the scattering wavelength. In the converse situation, the Doppler spectrum will display a Gaussian shape determined by the velocity dispersion within the scattering volume (Hanuise et al., 1993). There is also an intermediate case where neither Gaussian nor Lorentzian shapes can describe the entire Doppler spectrum. Typically, in this case, the first half of the corresponding autocorrelation function (ACF) is best fitted with a Gaussian curve, and the second half with a Lorentzian curve. However, as will be discussed, the relative contributions will vary depending on the correlation times of the plasma fluctuations.

Following the same steps that Gresillon et al. (1992) first showed, when looking at the backscatter signal at a time  $t$ , it can be represented in terms of its plasma susceptibility distribution

$$s(t) = \int_V \chi(\mathbf{r}, t) e^{-i\mathbf{k}\cdot\mathbf{r}} d\mathbf{r}^3 \quad (1.0)$$

where  $V$  is the observation volume and  $\mathbf{k}$  is the wave vector towards the antenna.  $\chi(\mathbf{r}, t)$  is the plasma dielectric susceptibility at the operating frequency. The autocorrelation of the backscattered signal can be written in terms of the signal frequency spectrum for the non-uniform “frozen-in” turbulent field

$$\langle s(t)s^*(t+\tau) \rangle = \frac{1}{n_c^2} \left\langle \int_V \int_V e^{-i\mathbf{k}(\mathbf{r}_1 - \mathbf{r}'_2)} [n(\mathbf{r}_1, t) d\mathbf{r}_1^3] \cdot [n(\mathbf{r}'_2, t) d\mathbf{r}_2^3] \right\rangle \cdot \langle e^{i\mathbf{k}\Delta(\mathbf{r}'_2, \tau)} \rangle \quad (1.1)$$

where  $n(\mathbf{r}, t)$  is the local fluctuating electron density,  $n_c$  is the plasma cut-off frequency, and  $\Delta$  represents the plasma displacement. This equation shows the relationship between spatial fluctuations in plasma density and the temporal ACF.

The first bracket in (7) is proportional to the form factor

$$\sum_{\mathbf{k}} = \frac{1}{N} \left\langle \int_V \int_V e^{-i\mathbf{k} \cdot (\mathbf{r}_1 - \mathbf{r}'_2)} [n(\mathbf{r}_1, t) d\mathbf{r}_1^3] \cdot [n(\mathbf{r}'_2, t) d\mathbf{r}_2^3] \right\rangle \quad (1.2)$$

where  $N$  is the total number of scattering particles. The form factor term represents the spatial component of the ACF.

The second averaged term is related to the probability distribution  $P(\Delta|\tau)$  of plasma displacements during time,  $\tau$ . The Fourier transform of probability distributions of plasma displacements can also be called the statistical ‘‘characteristic’’

$$\hat{P}^*(\mathbf{k}, \tau) = \langle e^{i\mathbf{k} \cdot \Delta(\mathbf{r}'_2, \tau)} \rangle = \int P(\Delta|\tau) e^{i\mathbf{k} \cdot \Delta} d\Delta \quad (1.3)$$

The scattered signal intensity is defined by the form factor and the time variation is in the ‘‘characteristic’’ of  $P(\Delta|\tau)$ .

The frequency spectrum,

$$S(\omega) = \int \langle s(t)s^*(t+\tau) \rangle e^{i\omega\tau} d\tau \quad (1.4)$$

is also defined from  $P(\Delta|\tau)$ , since

$$S(\omega) = \sum(\mathbf{k}) \hat{P}^*(\mathbf{k}, \omega) \quad (1.5)$$

where  $\hat{P}^*(\mathbf{k}, \omega)$  is the temporal Fourier transform of the probability distribution  $P$  (complex conjugate) space Fourier transform.

## 1.6.1 Scattering in the limit of long correlation length fluid turbulence

There exist two limiting cases for which correlation and spectrum can be related to a turbulent field. The first is obtained from a wavelength  $\lambda$  being small compared to the turbulence correlation length  $L_c$ . For any time  $\tau$  that is smaller than the correlation time  $T_c$ , then the displacement  $\Delta$  is given by

$$\Delta(\tau) = \mathbf{v} \tau \quad (1.6)$$

where  $\mathbf{v}$  is the local plasma velocity.

The displacement probability  $P(\Delta|\tau)$  is directly related to the fluid velocity probability distribution  $\mathbf{P}(\mathbf{v})$ . By combining equations (1.9) and (1.11) and approximating the integration over  $t$  by a delta function the resulting equation is

$$S(\omega) = \pi \sum(\mathbf{k}) \int \delta(\omega + \mathbf{k} \cdot \mathbf{v}) \mathbf{P}(\mathbf{v}) d\mathbf{v} \quad (1.7)$$

This is the familiar Doppler spectrum: the frequency distribution is determined by the distribution of fluid velocities along the  $\mathbf{k}$ -vector. This equation yields a Gaussian function.

## 1.6.2 Scattering in the limit of short correlation length

Where the observation wavelength  $\lambda$  is much larger than the turbulent motion correlation length  $L_c$ , the displacement probability  $P(\Delta|\tau)$  on the observation scale is that of a random walk, possibly convected at the uniform mean fluid velocity  $\mathbf{U}$ .

$$P(\Delta | \tau) = (4\pi D \tau)^{-3/2} \exp\left[-\frac{(\Delta - \mathbf{U} \tau)^2}{4D \tau}\right]$$

(1.8)

The coefficient  $D$  is the turbulent mass diffusion coefficient where

$$\frac{dn}{dt} = D \Delta n \quad (1.9)$$

In terms of the plasma motion correlation length  $L_c$  and time  $T_c$ , it is

$$D = \frac{L_c^2}{2T_c} \quad (1.10)$$

The associated “characteristic” is (for positive  $\tau$ )

$$\hat{P}^*(\mathbf{k}, \tau) = \exp[-k^2 D \tau] \exp[i\mathbf{k} \cdot \mathbf{U} \tau] \quad (1.11)$$

an exponentially decreasing function of time. The frequency spectrum is

$$S(\omega) = \frac{2k^2 D}{(\omega + \mathbf{k} \cdot \mathbf{U})^2 + [k^2 D]^2} \quad (1.12)$$

a Lorentzian profile, centered at the mean motion Doppler frequency. The profile frequency width  $\Delta f$  and angular frequency width  $\Delta\omega$  (half width at half height) are

$$\Delta f = \frac{\Delta\omega}{2\pi} = \frac{k^2 D}{2\pi} = \pi \left[ \frac{L_c^2}{\lambda} \right]^2 \frac{1}{T_c} = \pi \frac{L_c}{\lambda} \left[ \frac{k}{2\pi} \frac{L_c}{T_c} \right] \quad (1.13)$$

Note that this frequency profile is smaller than both the correlation frequency  $T_c^{-1}$ , and the (root mean square) fluctuating velocity Doppler frequency  $k (L_c/T_c)$ . This will have a Lorentzian shape.

### 1.6.3 Intermediate case

When the correlation length is of the same order as the observation wavelength, then a combination of the two previous cases is observed. The proportion of either Gaussian or Lorentzian shape in the observed ACF is determined by the correlation time. When the correlation time is larger than the sampling time  $t$  (i.e.  $T_c > t$ ), then the ACF will exhibit a Gaussian shape. However if the correlation time becomes shorter than the time  $t$  (i.e.  $T_c < t$ ), then the ACF will exhibit a Lorentzian shape. If this transition occurs in part of the observed plasma, then the best fit curve will be partly Lorentzian and partly Gaussian. However, neither curve will exhibit a good fit to the data. It will be assumed that this case also encompasses the occurrence where the correlation length of the plasma varies across

a volume such that both Gaussian and Lorentzian fits apply to different sections. This is of particular importance near the spectral width boundary.

## Chapter 2: The Instrumentation

### 2.1 SuperDARN

The Super Dual Auroral Radar Network (SuperDARN) currently consists of 10 HF radars located in the Northern Hemisphere and 6 HF radars located in the Southern Hemisphere. All SuperDARN radars are similar oblique sounding, coherent scatter radars sensitive to Bragg scatter from decameter scale irregularities in the ionosphere (Greenwald et al., 1995). The network is designed to have the radars working in pairs with common viewing areas which allow maps of 2-D high latitude plasma circulation to be obtained from the line-of-sight Doppler shifts observed by both radars (Greenwald et al., 1995). TIGER, located on Bruny Island, is currently the lowest latitude SuperDARN radar and, as such, it allows a view of the mid- and high-latitude ionospheres and the boundary between them. The HF radar at Halley base in Antarctica is almost opposite the south geomagnetic pole to TIGER, as seen in Figure 1.3.

SuperDARN radars employ a monostatic Tx/Rx array of 16 log-periodic antennas. An electronically controlled, time delay phasing matrix is used to steer the 16 antennas in 16 directions to cover a  $52^\circ$  azimuth region (Greenwald et al., 1995). Because the radars operate in the frequency range of 8 MHz to 20 MHz, the azimuthal resolution varies between  $2.5^\circ$  and  $6^\circ$  (Greenwald et al., 1995). The radars are designed to make a sweep through each of their 16 beams in a two minute period. In the case of TIGER, extra time is sometimes allocated to the beam aligned along the direction of the magnetic pole. The range resolution is determined by the pulse lengths, 100, 200, or 300 ms, which correspond 15, 30, and 45km. In the routine mode of operation, a pulse width of 45 km is used, and samples are taken at 70 ranges from a minimum range of 180 km through to a maximum range of 3330 km.



**Figure 2.0:** SuperDARN radars in the Southern Hemisphere (Courtesy of R.Barnes, Applied Physics Laboratory).

SuperDARN radars also employ a second array of 4 antennas which are used to determine the angle-of-arrival of the backscattered signal. To coordinate operation of all 16 radars, much of their operating time is allocated to “common time” (Greenwald et al., 1995). This is when all the radars run the same routine scans so that global data can be assimilated.

## **2.2 TIGER and Halley SuperDARN Radars**

### **2.2.1 The Tasman International Geospace Environment Radar (TIGER)**

The Tasman International Geospace Environment Radar (Dyson and Devlin, 2000) is located on Bruny Island (43.38°S, 147.23°E) off the south coast of Tasmania. This radar was constructed and began routine operations in 1999. The construction of the second HF radar located near Invercargill, New Zealand (Dyson et al., 2003), with an overlapping footprint over the Southern Ocean, is almost complete at the time of writing. This second

radar will enable estimates of the 2-D drift of plasma within the auroral oval and polar cap regions (which covers extensive regions of both open and closed field lines). TIGER records backscatter signals that result from Bragg scattering due to irregularities in the ionosphere, as well as waves propagating in the surface of the sea. These backscatter signals are obtained via different propagation modes through the ionosphere (Figure 2.2).



**Figure 2.1:** The TIGER radar consisting of 16 transmitting and receiving antennas in the main array and 4 receiving only antennas for the interferometer sub-array (courtesy of Danny Ratcliffe, Australian Antarctic Division).

The transmitting array consists of 16 log-periodic, 10 element antennas which are used to synthesise a  $4^\circ$  wide beam in azimuth when operating at 12 MHz. This frequency is adjusted depending on which frequency gives the most ionospheric backscatter, typically 14 MHz during the day and 12 MHz at night (Dyson et al., 2003). A further 4 receiving antennas are used to determine angle of arrival through interferometry.

TIGER uses the same array for both transmitting and receiving pulses, and it operates using a patented pulse sequence technique. For classical pulsed radars, pulses are sent at regular intervals, and an echo from the first pulse may return after the second pulse has been sent, and hence the echo will be incorrectly interpreted as a short range echo from the second pulse. Thus a longer period between pulses would be required. If the period is too long, though, the velocity of irregularities will be underestimated due to aliasing of

the echo Doppler shift. A clever way to avoid these problems is with a pulse sequence with different spacings between pulses, as seen in Figure 2.3.

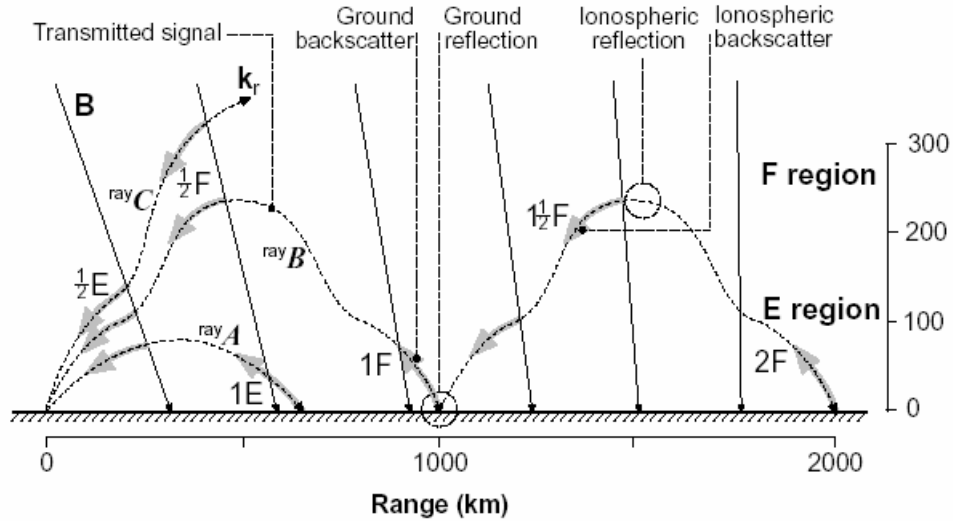


**Figure 2.2:** Propagation modes of signals in the ionosphere (courtesy of Steve Milan, 1997)

The current pulse set contains 7 pulses of length of  $300 \mu\text{s}$  which gives a 45 km range resolution. The pulses are separated by multiples of  $\tau$ , where  $\tau = 2400 \mu\text{s}$ , so that the autocorrelation function for the values of  $\tau$  from 1 to  $18\tau$  can be calculated (with the exception of  $16\tau$ ). This autocorrelation function (ACF) of the backscatter can then be Fourier transformed to obtain a Doppler spectrum.

The duration of a pulse set cycle is  $\sim 100 \text{ ms}$  and typical integration times are 3 s or 7 s. Hence during a 7 s sounding approximately 70 pulse sequences are emitted. The ACFs are averaged over the integration time and then this data is stored in a *.dat* file. This *.dat* file usually stores all complex ACF data for a two-hour block. Concurrently, the ACFs are analysed in real time by a program called FITACF (explained below) and stored in *.fit* files. These files can be used to create summary plots which typically display the power (dB), line-of-sight (LOS) Doppler velocity ( $\text{m s}^{-1}$ ), and spectral width ( $\text{m s}^{-1}$ ). This process is repeated during the integrations performed on each of the 16 radar beams. During discretionary time more beam 4 soundings are performed to increase the time

resolution. Beam 4 is chosen because it provides direct measurements of the zonal electric field.

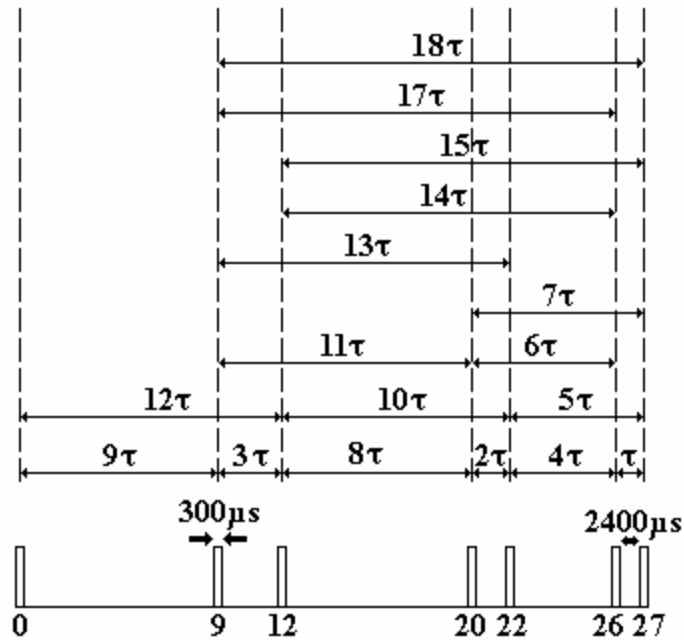


Figure 2.3: The pulse set presently employed by SuperDARN radars (Lester et al., 1998).

## 2.2.2 The Halley SuperDARN radar

A number of instruments used to measure the properties of the polar cap atmosphere are located at Halley Base in Antarctica ( $75.52^{\circ}\text{S}$ ,  $26.63^{\circ}\text{W}$ ). These include another HF radar, as seen in Figure 2.4, used to map ionospheric motions above Antarctica. This radar has been in operation since January, 1988, when it was originally paired with the Goose Bay HF radar in the Polar Anglo-American Conjugate Experiment (PACE) (Baker et al., 1989). Since then, another HF radar was built at Sanae, Antarctica, and its footprint overlaps the footprint of the Halley radar. The pair are known as the Southern Hemisphere Auroral Radar Experiment (SHARE), a tripartite experiment involving scientists from BAS, the Johns Hopkins University (USA), and South Africa (PUCHE, Potchefstroom, and the University of Natal). SHARE is able to determine the velocities

of ionospheric motions up to a maximum of  $\sim 2500 \text{ m s}^{-1}$  (UASD). All of these radars are key elements of the SuperDARN network, and operate in the same way as the TIGER radar. The Halley radar is of special significance to TIGER because the two radars are separated by  $174^\circ$  in longitude, and thereby provide a comprehensive view of anti-sunward drift across the southern polar cap.



**Figure 2.4:** The HF radar array at Halley Base in Antarctica (courtesy of British Antarctic Survey).

## 2.3 Pulse set technique and data analysis

### 2.3.1 Autocorrelation (ACFs) and “FITACF”

Many problems can occur when using pulsed radars to probe irregularities in the ionosphere. If a set of pulses is used with individual pulses being emitted at regular intervals, a serious problem arises when recording echoes from fast-moving irregularities at great ranges. Consider two pulses with separation  $\tau$ . Suppose also that there are two

regions of backscatter separated by distance  $c\tau/2$ . In this case, a backscattered signal from the first pulse echoing off the most distant region will coincide with an echo from the second pulse off the closer region. This problem is known as range aliasing, and inevitably arises when pulses have to be emitted in rapid succession to achieve the Nyquist frequency required to measure rapid motions.

An approach which minimises the problem of range aliasing is to have a pulse sequence that does not have any repetition of separations of multiples of  $\tau$ , as in Figure 2.3. However, other problems arise. With a multi-pulse sequence it is not possible to record an infinite number of lags in an autocorrelation function (ACF) without some redundant pairs, but for the lags up to 18 (excepting lag-16). Hence a 19 lag ACF is possible using the present sequence. The current SuperDARN pulse set permits calculation of all the lags up to  $18\tau$  with the exception of  $16\tau$ , with limited redundancy and range aliasing.

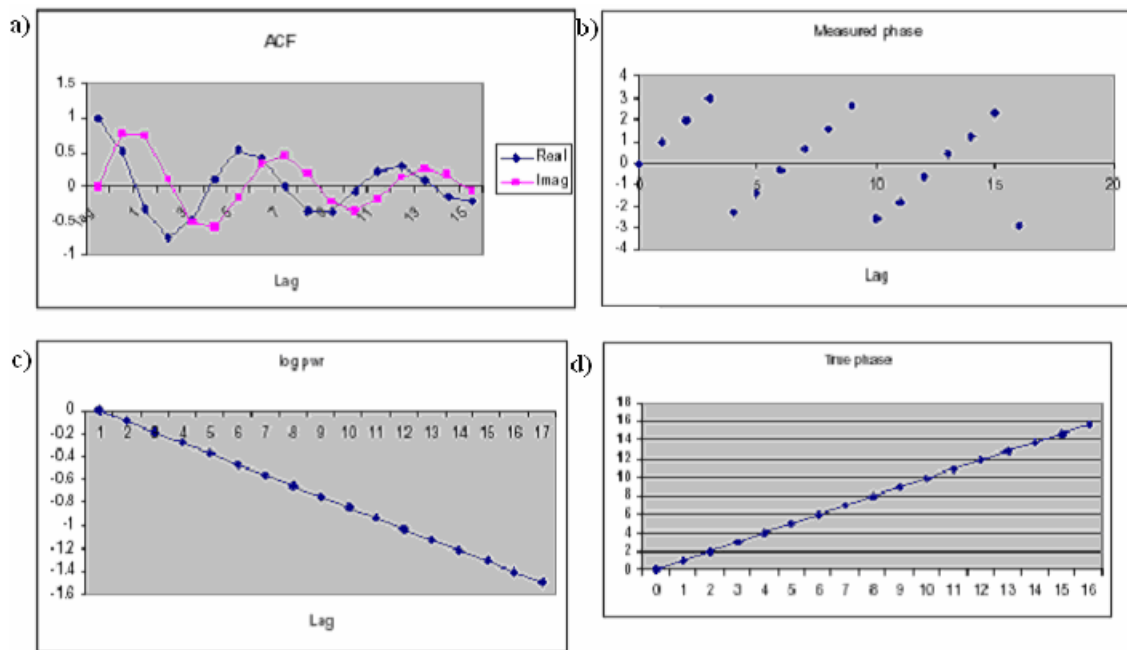


**Figure 2.5:** Example of an (a) ACF with decreasing power, (b) the typical type of measured phase, and (c) the log of the power of the ACF. As the log (power) is linear in this case, the spectra will have a Lorentzian fit. (d) The true corrected phase of an ideal ACF obtained by shifting the curves in (b).

A complex amplitude is recorded each time the receiver digitises an echo. That is, the component in-phase with the receiver clock ( $I$  component) and the component in

quadrature (90° out of phase) with the receiver clock ( $Q$  component) are obtained. This allows creation of a single complex number of the form  $I + iQ$  representing the received wave (Villain et al., 1996). When looking at an ACF corresponding to a Doppler spectrum with a single peak, the maximum power should be recorded at lag-0, with each subsequent lag decreasing in power, as in Figure 2.5a.

Lags do not always behave in the expected way and are labelled as “bad lags” (i.e. lags that are not considered useful for subsequent analysis). To calculate the individual lags of an ACF, take the signal received from an arbitrary range corresponding to the first pulse,  $0\tau$  ( $S_0$ ). Next, take the signal received from the same range corresponding to the ninth pulse,  $9\tau$  ( $S_9$ ). Hence the autocorrelation value for lag  $9\tau$  is then calculated from  $A_9 = S_9 \times S_0^*$ , where the  $S_0^*$  represents the complex conjugate of  $S_0$  (Baker). By using different combinations of pairs, the values for the ACF can be calculated for every lag.

FITACF is a program that is run at the site of each radar and is used to fit curves to the ACFs as they are created in real time. The ACF will decorrelate as the lag increases, and this decorrelation can be modelled by the log of the power as either a linear (Lorentzian, as seen in Figure 2.5c) or a parabolic (Gaussian) function (Greenwald et al., 1985). FITACF performs least squares fits to the data and computes values for many different parameters, including, but not limited to, power, line-of-sight velocities (LOS), and spectral width, all of which are obtained using Lorentzian and Gaussian fits. Errors in all of these parameters are calculated, including the spectral width errors and the standard deviation of the least squares fits (Lorentzian and Gaussian). An ACF can be transformed to a Doppler spectrum using the Fast Fourier Transform (FFT). FITACF returns reasonably accurate parameters when the corresponding Doppler spectrum is dominated by a single peak.

The main parameters (power, LOS, and spectral width) are calculated as follows (Baker et al., 1995). The power component is determined by the signal-to-noise ratio of lag-0 in the ACF. The LOS velocities are calculated from the Doppler velocity equation

$$\langle v \rangle = \frac{c\omega}{4\pi f} \quad (2.0)$$

where  $f$  is the radar frequency, and the factor of 4 comes about because the signal travels along the path twice (out and back). The  $\omega$  term is the mean Doppler frequency and is determined by a least squares fit to the phases of the ACF. For a given lag, the ACF can be expressed as

$$A_k = P_k e^{i\phi_k} \quad (2.1)$$

where  $P_k$  is the power of lag  $k$  and the  $e^{i\phi_k}$  component represents the phase. For an ACF characterised by only a single frequency, the phase corresponding to the  $k^{\text{th}}$  lag is simply  $\phi_k = \omega k \tau$ . By using a least squares fit of the phases,  $\phi_k$ , to a straight line passing through the origin, as seen in Figures 2.5b and 2.5d, it is possible to find the Doppler frequency shift  $\omega$ .

To estimate the Lorentzian spectral width, the ACF is considered to be of the form

$$|A_k| = C e^{-\lambda k \tau} \quad (2.2)$$

Where  $C$  is a constant and  $\lambda$  is the decay parameter. A least squares fit between  $\log_e(A_k)$  and  $k\tau$  is performed. The  $y$  intercept of this line will determine  $C$  which is called the  $\lambda$  power, and the value of the gradient determines the decay time  $\lambda$ . A Fourier transform of the ACF will yield the relationship between the spectral width at half maximum and the decay parameter. The Fourier transform is

$$\int_{-\infty}^{+\infty} C e^{-i\omega t} e^{-\lambda|\tau|} = \frac{2C\lambda}{\lambda^2 + (\omega - \omega')^2} \quad (2.3)$$

The full width at half maximum (the spectral width) of a spectrum of this form is  $2\lambda$  rad  $s^{-1}$ . Again, this is converted to a Doppler velocity using the equation

$$\Delta v = \frac{2c\lambda}{4\pi f} \quad (2.4)$$

Whilst this method of estimating the spectral width is good when only one frequency shift is involved (i.e. a single-peaked spectrum), it is not accurate if multiple peaks are present.

A similar analysis is applied to estimate the Gaussian spectral widths.

### 2.3.2 Summary plots

In this study, we will present the results saved to *.fit* files in the form of summary plots, a standard way of displaying the parameters measured by the radar. As shown in Figure 2.6, a summary plot consists of three variables plotted against group range and time in separate panels. There are four basic plot variables that this version of summary plotter is capable of producing.

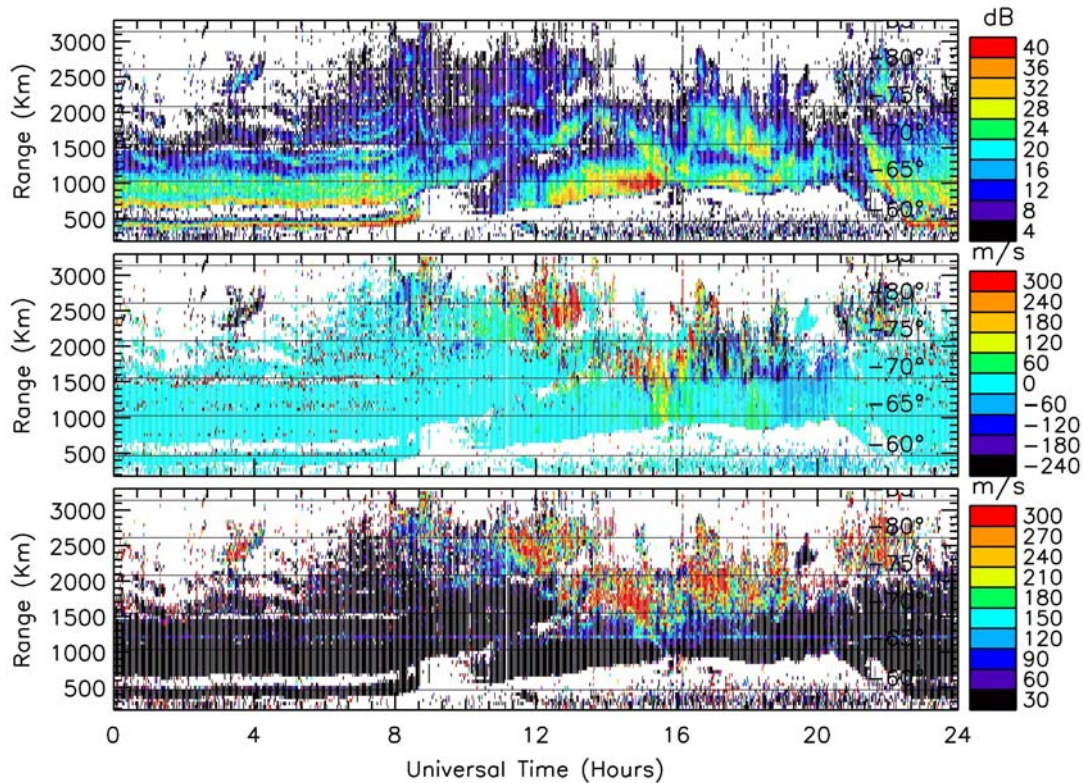


**Figure 2.6:** Summary plot of power (dB) (top panel), LOS velocities ( $\text{m s}^{-1}$ ) (middle panel), and Lorentzian spectral width ( $\text{m s}^{-1}$ ) (bottom panel) for TIGER beam 4 on 30<sup>th</sup> April 2000.

The first parameter is the power, or signal to noise ratio, on a logarithmic scale (dB), and it is a measure of how much of the HF power is backscattered to the radar. The second parameter shown is the LOS velocity. The LOS velocity component is a measure of the

motion of the ionospheric irregularities either towards or away from the radar. An irregularity moving transverse to the beam will have a LOS velocity of zero. The third parameter is the spectral width (Lorentzian). This is a measure of the full width at half maximum of the peak in a corresponding single-peaked Doppler spectrum. Strictly speaking though, it is simply a measure of how rapidly the ACF decorrelates.

Elevation angles are another important parameter which can be represented in summary plot form. By measuring the difference in arrival times of echoes between the main array of 16 antennas and the subarray of 4 receiver antennas, the angle of arrival can be estimated. Many other parameters stored in the *.fit* files can be displayed in summary plot form.

### 2.3.3 TGRaw

TGRaw is a program written by Colin Waters at the University of Newcastle, and was written to display the raw ACF data (i.e., not processed by FITACF) saved to *.dat* files. The ACFs recorded for individual times, beams, and ranges can be chosen for display. TGRaw can also display the corresponding Doppler spectra obtained by applying a Fast Fourier Transform (FFT) to the ACFs. This allows users to better characterise the Doppler characteristics of individual ACFs and spectra, and judge the quality of FITACF results.

## 2.4 Multi-peaked spectra

When looking at the Doppler spectra of most ionospheric scatter, there is usually an isolated single peak representing the velocity of the irregularities inside the region being observed. Sometimes though, there may be more than one peak in the Doppler spectra due to irregularities travelling in more than one direction inside the scattering volume, or possibly due to simultaneous readings from the top and bottom of the electrojet layer

(Danskin et al., 2004). These spectra are known as multi-peaked spectra. Whilst this type of spectra are known to occur, the default data analysis performed by SuperDARN radars is not adequate to determine where and when they will occur.

The main problem concerning the detection of multi-peaked Doppler spectra resides in the way that the data is manipulated from received pulses to form an ACF, and its subsequent interpretation by FITACF. As previously discussed, when the ACF is analysed, if a lag's power is larger than a previous lag's power, then the lag is considered a bad lag because it does not conform to a single peaked spectrum (Baker). When looking for multi-peaked spectra, we would expect to see a lag power greater than the previous lag which would signify the presence of a second peak. For this reason, FITACF is not appropriate for analysing multi-peaked spectra. Instead, an approach using a statistical model known as the Burg model (Burg, 1975) may be more appropriate. The Burg spectrum method is a type of maximum entropy method. It is an autoregressive method that fits the data with a statistical model (Danskin et al., 2004).

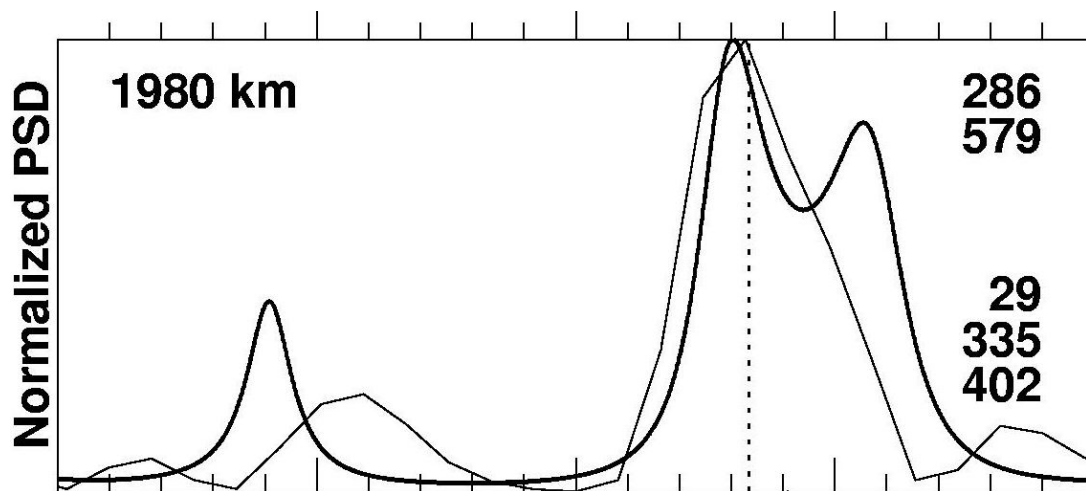


**Figure 2.7:** The normalised power spectrum density (PSD) for range gate 40 of the TIGER beam 4 at 1315 UT on 10<sup>th</sup> December, 1999. Shown are the Doppler spectrum obtained from a Fourier transform of a standard ACF (thin line), and the Burg spectrum of the same data (thick line). The range of the data is shown at the top left, and the velocities of the two major peaks at top right. The power (dB), LOS Doppler velocity ( $\text{m s}^{-1}$ ), and spectral width ( $\text{m s}^{-1}$ ), as calculated by FITACF, are shown at bottom right (top to bottom).

As seen in Figure 2.8, this method produces much smoother Doppler spectra than the spectra obtained from the Fourier transform of the ACF. Looking at Figure 2.8, the Burg analysis of the data shows a contrasting picture to the Doppler spectrum calculated from the ACF. Where previously a single, clear peak dominated, there are now 3 fairly distinct peaks that form a convincing multi-peaked spectrum. A more in-depth analysis of these multi-peaked spectra will be continued in a later section.

## Chapter 3: Movement of the deep polar ionosphere

### 3.1 Antisunward drift due to magnetic reconnection

The polar ionosphere is defined as the region poleward of the open-closed magnetic field line boundary, located approximately poleward of 70-75° geomagnetic latitude. The deep polar ionosphere is the region approximately poleward of 80° geomagnetic, and has been poorly studied because of its geographic remoteness. Plans for new coherent scatter radars in these regions as an extension of SuperDARN known as PolarDARN, have commenced in the northern hemisphere. Such experiments to view the deep polar ionosphere are also planned for Antarctica in the near future. The mobile, Advanced Modular Incoherent Scatter Radar (AMISR) has the ability to be relocated at any time and holds the key to observing these regions with the ability to relocate the radar at any time.

There are many reasons for the movement of irregularities in the deep polar ionosphere. While many of these are due to small scale processes, there is one form of large scale movement that dominates the flows of irregularities in this region. These flows are due to plasma movement perpendicular to magnetic field lines. The motion may be considered as the motor effect of the cross-polar electric field mapped down from the magnetosphere.

In the accepted model of magnetospheric convection, reconnection (or merging) of the interplanetary and geomagnetic field lines partially opens the Earth's magnetic field to the solar wind. For this to happen, the field lines must be oppositely directed: a southward interplanetary magnetic field (IMF) is thus needed to open the Earth's closed dayside magnetic fields. This is known as the anti-parallel merging hypothesis.

Antisunward magnetospheric convection is produced when the newly opened field lines are swept over the polar caps at a speed determined by the turbulent magnetosheath flow. The dawn-to-dusk solar wind electric field  $E = -v_{sw} \times B_{sw}$  maps down the open field lines,

driving an antisunward  $\mathbf{E} \times \mathbf{B}$  drift of plasma in the F-region ionosphere. When the northern and southern hemispheric field lines are stretched into a magnetic tail by the solar wind, they eventually reconnect with each other downwind near the equatorial plane of the magnetosphere. The associated magnetospheric convection maps to a dusk-to-dawn electric field and sunward plasma flow in the auroral ionosphere: the familiar two-cell pattern of ionospheric convection is formed, as seen in Figure 3.1.

There are two main patterns of plasma convection, those associated with IMF southward conditions, and those due to IMF northward conditions. In this study, only the case associated with IMF southward conditions will be considered. Figure 3.1 shows an idealised representation of the associated two cell convection pattern. The case of IMF northward conditions is more complex, and only a brief description will be given.

The convection pattern associated with IMF northward conditions is confined to higher latitudes and has velocities smaller than in the case of the southward IMF. Reconnection in this case is only possible between the IMF and already open field lines poleward of the cusp, and because of this, three or even four cell ionospheric convection patterns can occur. While some of the possible three and four cell convection patterns can resemble the two cell model, this topic is at the cutting edge of theoretical research, and is not considered in this thesis.

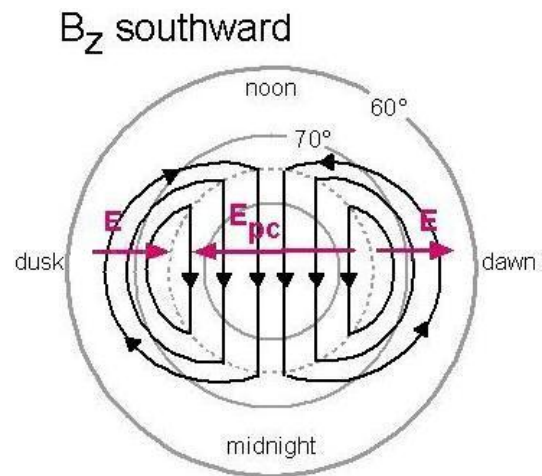


**Figure 3.1:** A view of the Northern polar region from above, consistent with the magnetic field,  $B_z$ , into the page, the polar cap electric field in the dawn-to-dusk direction, and the resultant velocity of the plasma in the noon to midnight direction ( $\mathbf{v} = \mathbf{E} \times \mathbf{B}$ ). The electric fields in the auroral zone drive the sunward flow of plasma back into the dayside ionosphere (Spaceweb, 1998).

## 3.2 Experimental design and data selection

The purpose of this study was to observe antisunward drift in the southern polar region and to look at the deep polar region with both TIGER and Halley incoherent scatter HF radars.

To look at the convection patterns as described in the previous section, a way to view flows in the ionosphere in this region was needed. For this study, the TIGER and Halley coherent backscatter HF radars were used. Since TIGER and Halley are on opposite sides of the southern magnetic pole, there is an ideal opportunity to look at antisunward drifts, primarily in the noon to midnight sectors, in this region. The purpose of this investigation was to first look at whether there was correlation in the readings from TIGER and Halley supporting antisunward drift especially in the deep polar region above  $75^\circ$  latitude. This was to be done by looking primarily at the noon and midnight sectors in both TIGER and Halley data for a set period where the irregularities should exhibit this drift. Looking at this antisunward drift across the southern polar ionosphere was also a way to test the data being collected by TIGER and Halley, and that it followed standard models of the ionosphere so that further investigations using data from these radars could be justified.

To look at the antisunward drift in the southern polar region, a time was to be chosen for observations such that optimal viewing in this region must occur. A study of periods where maximal occurrence of backscatter echoes and high numbers of magnetic storms and substorms occurred revealed the equinox in March/April as the ideal time to look at the antisunward drift. That is why the month of April was chosen. The year of the study was chosen to be as close to sunspot maximum as possible and since TIGER was still only new in 1999 with some inconsistent data periods in April 1999, the month of April 2000 was chosen for the study. Due to the large size of the files to be analysed (that had to be sent from the British Antarctic Survey) in this study, and that this was only a brief look at the drift regions, only one month of data was chosen to be examined.

While there were still a large number of days where large regions of time could be observed, 4<sup>th</sup> April contained the entire data for both TIGER and Halley. For this reason, 4<sup>th</sup> April was used as the primary data set in this study.

### **3.3 Halley and TIGER observations of antisunward drift**

The Halley and TIGER radars are capable of simultaneously observing antisunward drift in the deep polar cap ionosphere. In this section, the first observations identifying this capability are shown. Figures 3.2 and 3.3 show the summary plots of Halley and TIGER data for the 4<sup>th</sup> April 2000, respectively. The Halley data is the beam 8 data due to beam 8 looking along the magnetic meridian and hence looks over the greatest number of latitudes. The TIGER data uses beam 4 data for the same reason. Both plots show sea scatter/ground scatter as determined by FITACF.

The Halley summary plot contains various periods of interest to this study. First to note is the very high ( $>300 \text{ m s}^{-1}$ ) Doppler velocities towards the radar during the night time periods (0000 – 0300 UT and 1930 – 2400 UT). These echoes are predominantly  $\frac{1}{2}$  hop echoes from both E and F regions. The second region to investigate is the dusk to dawn interval between 0300 and 1830 UT which contains high Doppler velocities away from the radar, and in the direction of the TIGER radar. Of particular note is the scatter between 0800 and 1330 UT. This scatter appears to be moving across the polar cap towards TIGER and will be considered further in the analysis.

Looking at the TIGER summary plot, there are similar periods of interest when looking for evidence of antisunward drift. In the nighttime period, there are strong Doppler velocities coming towards the radar, both in the E and F regions, and both from  $1\frac{1}{2}$  hop (0730 – 1230 UT, 2000 km) and  $\frac{1}{2}$  hop (1300 – 1800 UT, 0500 – 2000 km) scatter. It is interesting to note that the region of  $1\frac{1}{2}$  hop echoes are at a range that does not quite overlap the scatter seen by the Halley radar but seem to have come from Halley.

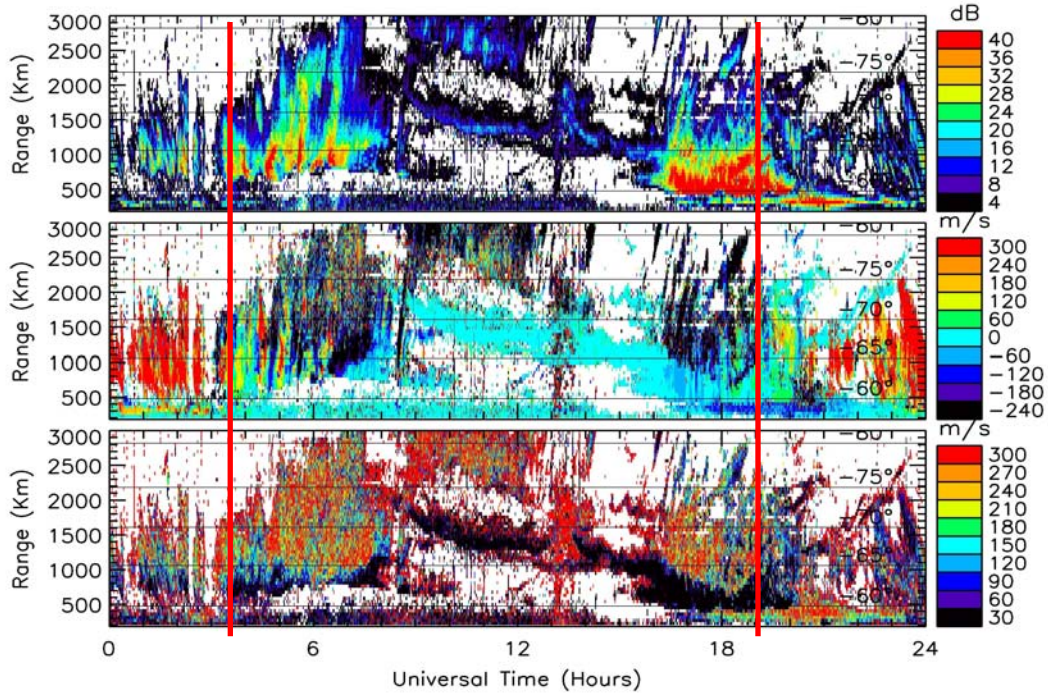


**Figure 3.2:** Summary plot of Halley, beam 8 observations for the 4<sup>th</sup> of April 2000, with power (dB) (top panel), line-of-sight Doppler velocities ( $\text{m s}^{-1}$ ) (middle panel), and Lorentzian spectral width ( $\text{m s}^{-1}$ ) (bottom panel). The first vertical red line represents magnetic dawn (06 MLT) and the second vertical red line represents magnetic dusk (22 MLT).

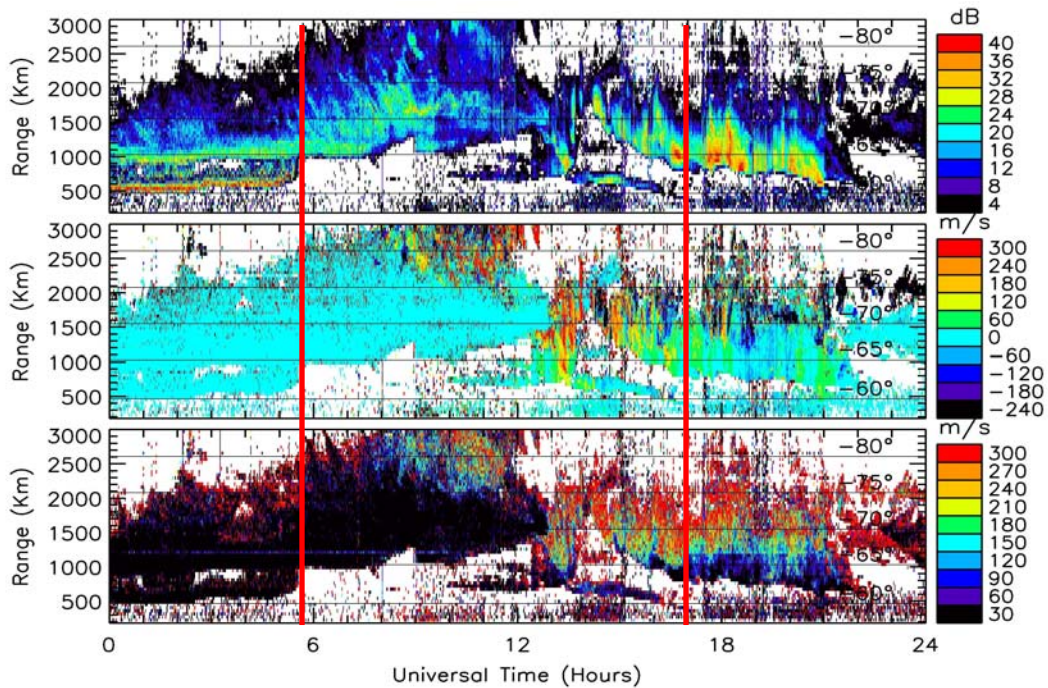


**Figure 3.3:** Summary plot of TIGER, beam 4 observations for the 4<sup>th</sup> of April 2000, with power (dB) (top panel), line-of-sight Doppler velocities ( $\text{m s}^{-1}$ ) (middle panel), and Lorentzian spectral width ( $\text{m s}^{-1}$ ) (bottom panel). The first vertical red line represents magnetic dusk (20 MLT) and the second vertical red line represents magnetic dawn (06 MLT).

During the daytime period, there are some echoes showing Doppler velocities away from the radar (2000 – 2400 UT). Again, these Doppler shifts are in basic agreement with the two cell convection model. The echoes seen prior to 0800 UT are primarily sea scatter with some hints of overlapping ionospheric scatter. This scatter is not relevant here. Considered together, these Doppler shifts are in basic agreement with the two-cell convection model.

### **3.4 Halley and TIGER observations of the deep polar ionosphere**

In the deep polar ionosphere, increases in the electron densities lead to enhancements in this region known as polar cap patches. These polar cap patches are seen during periods of disturbed conditions and tend to be stronger near sunspot maximum. Due to the large gradients in and around these patches, irregularities form on the boundaries of these structures. Smaller patches can be caused by an increase in the flow of the solar wind and sudden changes in the IMF (Anderson et al., 1988). This can cause the patches to detach from the dayside cusp region and drift across the pole with the according to the antisunward drift.

When looking at the deep polar ionosphere, the region of particular note in Figures 3.2 and 3.3 are those above  $75^\circ$  latitude. Ionospheric scatter in this region in both the Halley and TIGER summary plots occurs between the times of 0730 and 1300 UT.

This is a strong argument for antisunward drift in this region. One further way of checking this drift is in closer analysis of the region mentioned above corresponding to the data received from Halley as seen in Figure 3.4. In Figure 3.4, the region between 1500 and 3000 km from the radar has been enlarged from Figure 3.2 corresponding to the times from 0700 – 1300 UT. In Figure 3.4 a large region of fast moving (high Doppler velocity) irregularities are seen steaming away from Halley in the middle panel, across the geomagnetic pole towards TIGER.

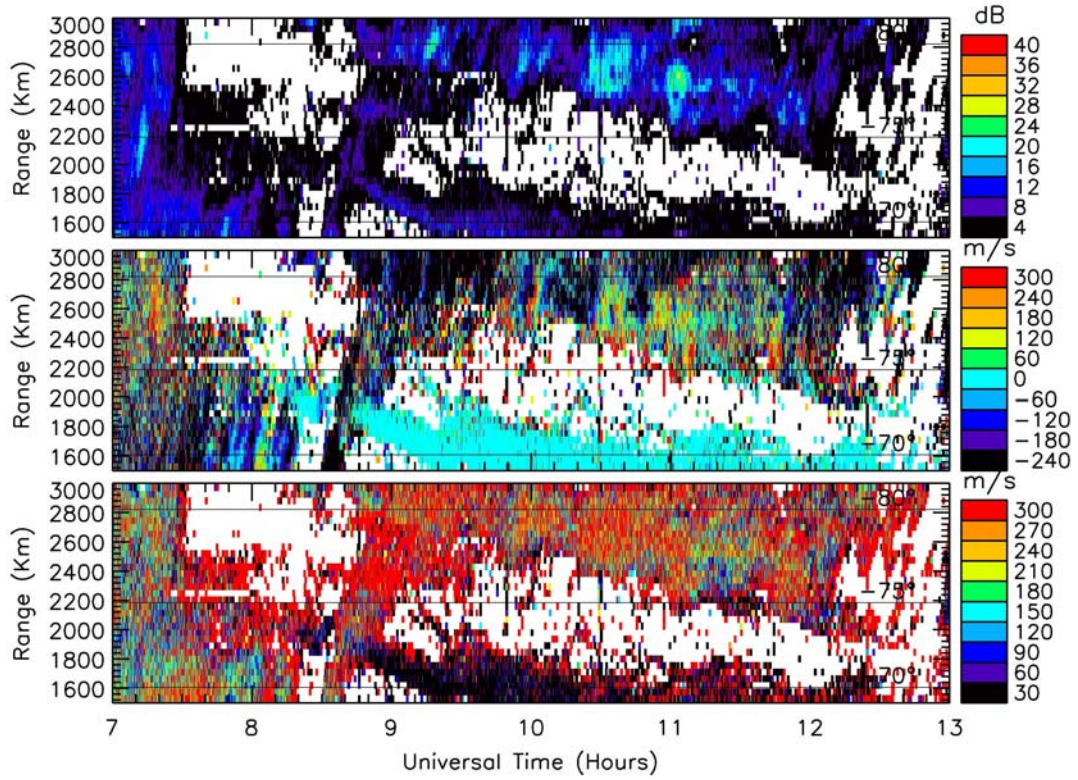


Figure 3.4: An enlargement of the region of  $1\frac{1}{2}$  hop echoes in Figure 3.2

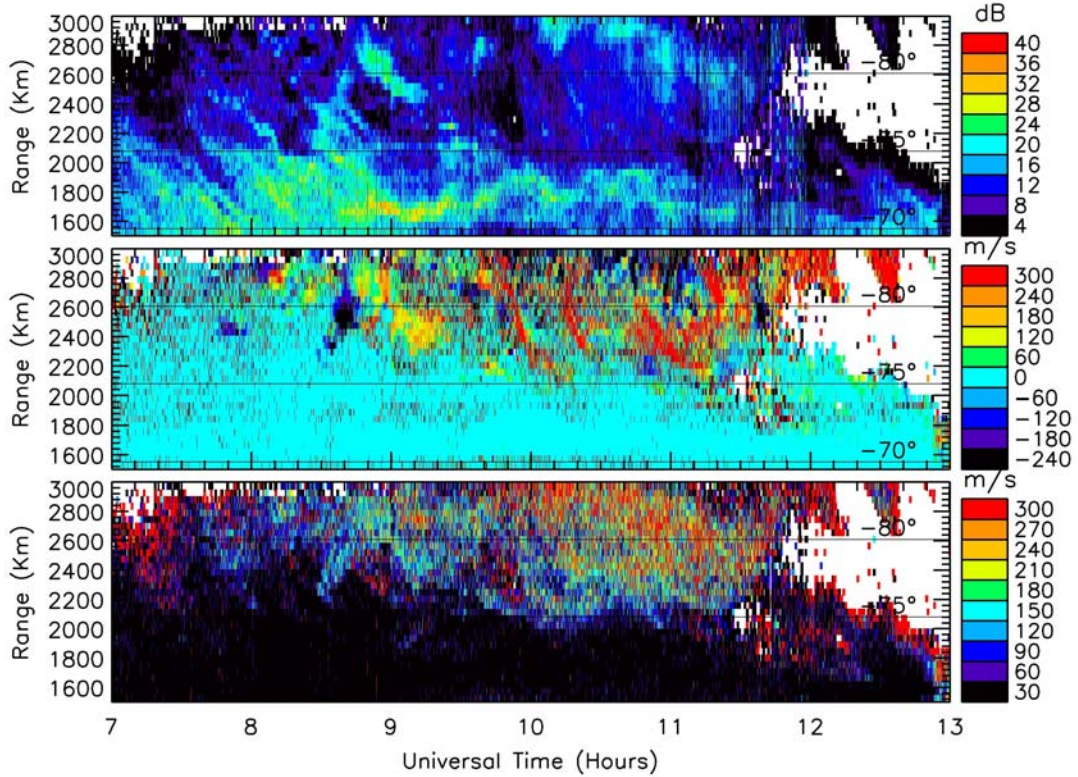


Figure 3.5: An enlargement of the region of  $1\frac{1}{2}$  hop echoes in Figure 3.3

The TIGER data corresponding to this same area can be seen in Figure 3.5. The TIGER data in Figure 3.5 shows irregularities streaming towards TIGER at the same time.

While these radars do not have overlapping footprints, what is being seen is the movement of a large enhancement (polar cap patch) consisting of irregularities moving from the Halley radar field of view across the polar-cap and into the TIGER radar field of view.

This region of irregularities contains an interesting difference when looking at Figures 3.4 and 3.5. Here the spectral widths (bottom panel) observed by Halley far exceed the values measured by TIGER. This region is not overlapping but in fact has a separation of a few degrees latitude across the polar cap. While many hypotheses could be made about this region, there are no conclusive facts to prove one or another is true. If a radar had a field of view encompassing this region, then this discrepancy could be resolved but at this time there are no other independent views of the ionosphere in this region.

The irregularities seen moving across the polar region in Figures 3.4 and 3.5 provide substantial evidence that the antisunward drift across the polar region can be observed using the TIGER and Halley radars and of the importance in obtaining a view of the deep polar ionosphere to complete the coverage in this region. This result also gives conformation of the data being gathered by these radars, so that when examining further phenomena which have not been fully investigated previously, the backscatter being observed gives a true account of the region. The use of TIGER and Halley data in terms of a model of the southern polar region, with respect to the movement across the polar region, exhibits a good fit to the theoretical model.

## Chapter 4 – Spectral widths, Lorentzian or Gaussian?

### 4.1 Why use Lorentzian or Gaussian curves?

When considering HF backscatter detected by SuperDARN radars, the spectral width is determined by how rapidly the ACF power decays with lag number – the more rapid the decay, the larger the spectral width. As described earlier, according to collective wave scattering theory, the ACFs will be best fit by a Lorentzian or Gaussian curve, or a combination of both. Previous SuperDARN studies have shown that Lorentzian type Doppler spectra are usually prevalent throughout the polar cap ionosphere. Hence the use of Lorentzian spectral widths is favoured for routine analysis of most SuperDARN radar data. Ideally, though, the spectral width for every individual ACF should be plotted on the basis of whether the Lorentzian or Gaussian fit was better.

Part of this study was to examine the Gaussian and Lorentzian spectral widths recorded by TIGER, and to determine which kind of spectral width was more representative of the plasma characteristics. Perhaps the importance of Gaussian spectral widths was being overlooked. To examine the differences between Lorentzian and Gaussian spectral widths, and to decide which type of spectral width better fits the observed ACFs, a way to compare these two types of spectral width was needed. Summary plots are an effective way of displaying the multi-dimensional radar data recorded by SuperDARN radars throughout extended regions of time and range. In the following sections, we use them to analyse differences between the Gaussian and Lorentzian spectral widths.

### 4.2 Lorentzian versus Gaussian spectral widths

The data displayed in summary plots is derived from real-time FITACF analysis of the coherently averaged ACFs recorded by the radar. Whilst a large number of parameters are created by FITACF, most of these are usually not displayed in the form of summary

plots. These include separate summary plots of the Lorentzian and Gaussian spectral widths. Whilst these summary plots can not determine which of the two spectral types best fit the data, it is a good way to reveal how they affect the appearance of the spectral width features in space and time.

Summary plots of the Lorentzian and Gaussian spectral widths are shown in Figure 4.1. It can be seen that the Lorentzian spectral widths and the Gaussian spectral widths determine the same basic areas of high and low spectral widths. However, there is a major difference between the two plots. On a statistical basis, the Gaussian spectral widths are more than  $30 \text{ m s}^{-1}$  larger than the Lorentzian spectral widths. The FITACF process needs to be modelled to understand all of its idiosyncrasies, but it is apparent the Gaussian spectral widths are systematically larger than the Lorentzian spectral widths for the same fitting errors.

According to Prof. J.-P. Villain (private communication, 2004), one of the principal architects of the pulse set/FITACF technique, the Gaussian spectral widths are estimated by performing a least squares linear fit using logarithmic-logarithmic coordinates, whereas the Lorentzian spectral widths are determined using semi-logarithmic coordinates. The Gaussian fit becomes a parabola, whereas the Lorentzian fit becomes a straight line. For the latter, a relatively small departure of the fit for low values of the power approaching noise gives large errors. Hence the errors of the Lorentzian spectral widths should be larger. Moreover, the fitted parameters are multiplied by a coefficient of 2 to estimate the Lorentzian spectral widths and 3.3 to estimate the Gaussian spectral widths (Villain et al., 1996).

These systematic problems with the FITACF method should not be confused with the characteristics of the plasma fluctuations implied by the theory of collective wave scattering. When the Lorentzian spectral shape best fits the data, the correlation length of the plasma fluctuations is less than the radar wavelength, and the corresponding spectral widths under-estimate the velocity fluctuations assuming velocity dispersion by as much as a ratio of  $2/kL_c$ , where  $kL_c$  is the correlation length (cf. section 1.6, (Hanuise et al.,

1993)). Hence, even when the Lorentzian spectral shape best fits the data, the absolute spectral widths estimated using a Gaussian spectral shape may be more representative of the absolute values of velocity dispersion.

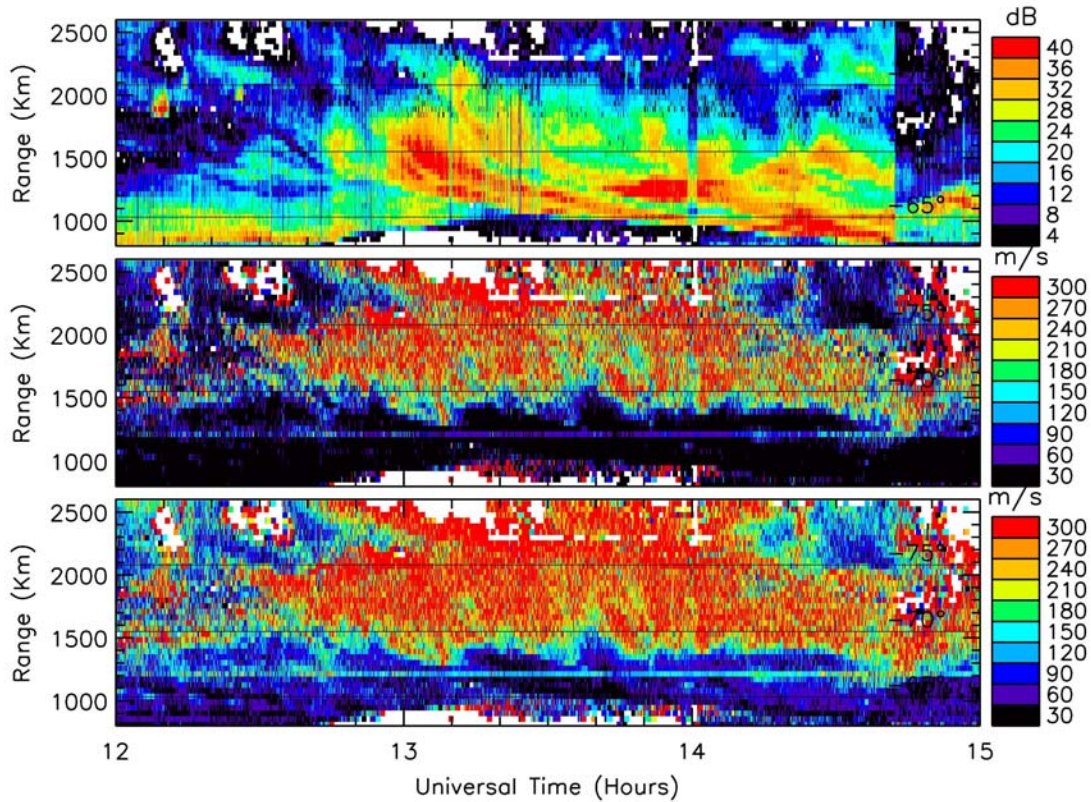


**Figure 4.1:** A summary plot of TIGER, beam 4, for the 10<sup>th</sup> of December 1999 showing power (dB) (top panel), Lorentzian spectral widths ( $\text{m s}^{-1}$ ) (middle panel), and Gaussian spectral widths ( $\text{m s}^{-1}$ ) (bottom panel).

The key to determining whether Lorentzian or Gaussian fits best represented the data was to compare the standard deviations of the fits of each. The spectral width type which better approximated the data would have a smaller value for its standard deviation. As explained, the spectral width errors themselves may be over-estimated for the Lorentzian fits, and are not a reliable indication of goodness of fit.

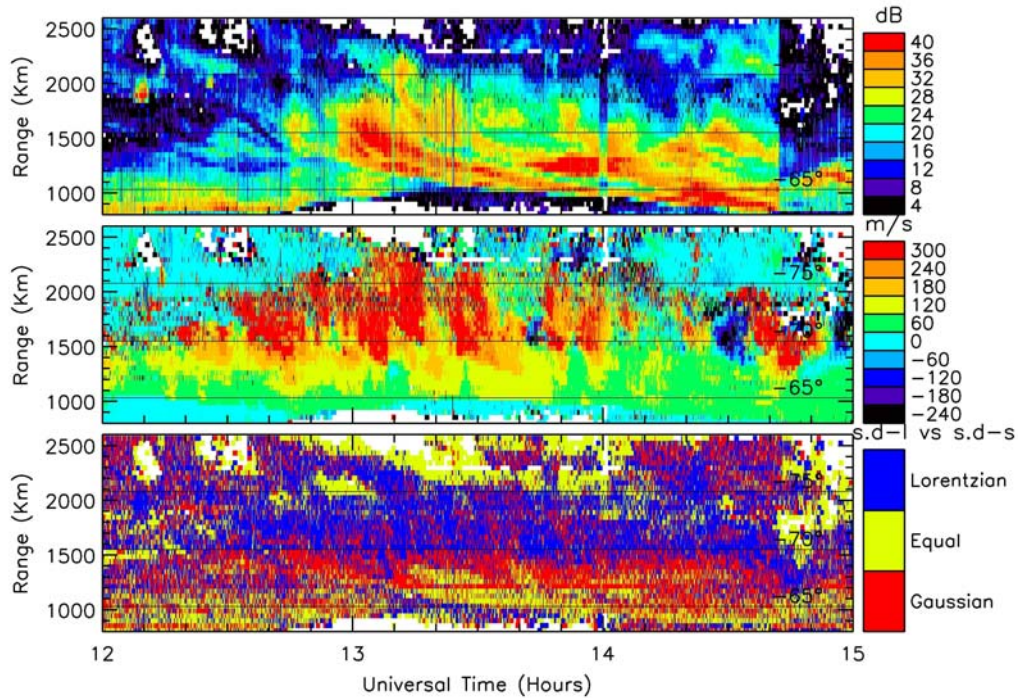


**Figure 4.2:** A summary plot of TIGER, beam 4, for the 10<sup>th</sup> of December 1999 showing (top panel) power (dB), (middle panel) line-of-sight Doppler velocities ( $\text{m s}^{-1}$ ), and (bottom panel) Lorentzian standard deviation versus Gaussian standard deviation. The bottom panel displays blue when the Lorentzian standard deviation has a lower value, red when the Gaussian standard deviation has a lower value, and yellow when neither Gaussian nor Lorentzian provided a better fit.

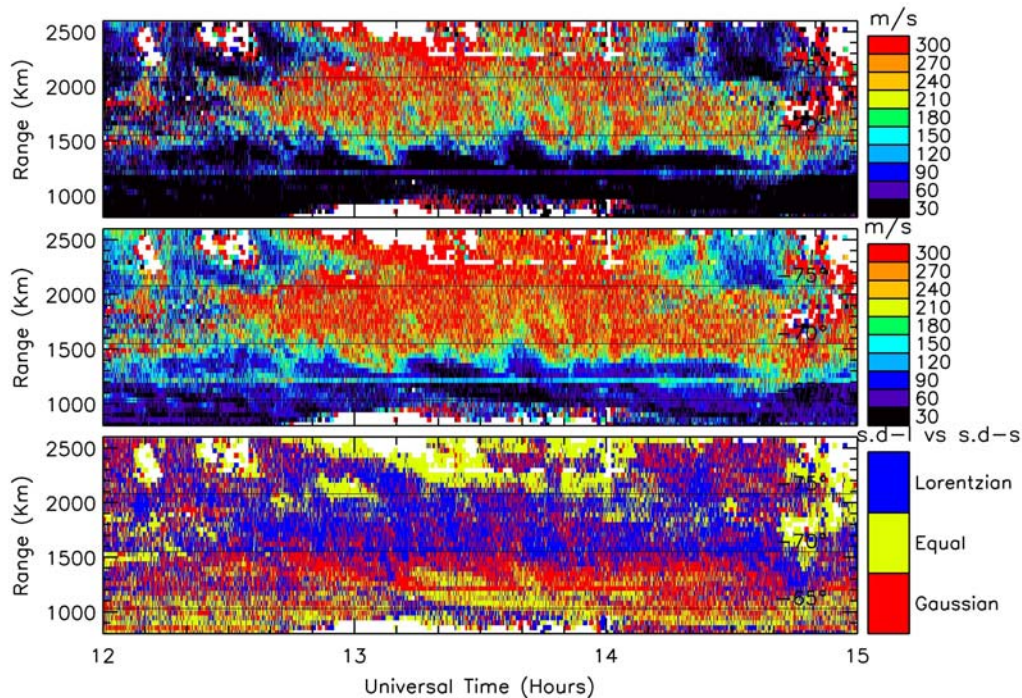


**Figure 4.3:** A summary plot of TIGER, beam 4, for the 10<sup>th</sup> of December 1999 showing (top panel) Lorentzian spectral widths ( $\text{m s}^{-1}$ ), (middle panel) Gaussian spectral widths ( $\text{m s}^{-1}$ ), and (bottom panel) Lorentzian standard deviation versus Gaussian standard deviation.

We created a summary plot that took the standard deviations of the Gaussian and Lorentzian fits, and plotted which of the two values had the lowest value within 20% for errors. If the two standard deviations were the same within 20%, then neither fit was deemed better. As shown by Villain et al. (1996), an increase in this threshold decreased the number of Gaussian and Lorentzian pixels shown, but overall did not change the structure. For this reason and to allow a better view of the individual properties of this data, the threshold was removed for these plots. Each of the pixels which corresponded to a better Lorentzian fit were plotted in blue, and each of those with a better Gaussian fit were plotted in red. When neither Gaussian nor Lorentzian fits were better, the pixels were plotted in yellow. This can be seen in the bottom panel of Figures 4.2 and 4.3. In these plots, a horizontal line can be clearly seen at  $\sim 1215$  km. This line corresponds to a bad range and should be ignored.

In Figure 4.2, the power and line-of-sight Doppler velocities were plotted so as to compare with the standard deviation plot. Comparisons between the plots in Figure 4.2 shows that the standard deviation plot appears to have no direct relationship with the power, whereas a distinct drop in line-of-sight Doppler velocities can be seen at the range of  $\sim 1500$  km.

In Figure 4.3, there appears a close correlation between the spectral widths and the standard deviation plot. The area of most significance is a distinct boundary between the Lorentzian and Gaussian standard deviation zones of best fit at ranges  $\sim 1400$  to  $1500$  km which corresponds closely to the spectral width boundary. Further analysis of the standard deviation with respect to the variables mentioned above could be achieved using scatter plots to look more closely at areas of interest so as to determine the full extent of the relationships between them. Due to time constraints this was not performed in this study.

There are some features in the standard deviation plot (bottom panel) in Figure 4.3 that need further attention. There appear to be near vertical lines of Gaussian pixels in the Lorentzian dominant region that will need to be looked at further. There also appear to be

regions of where the Gaussian fit competes with the Lorentzian fit. These can be seen in the regions of 1200–1245 UT and also 1415 – 1445 UT at ranges greater than 2000 km. Scatter plots of the distribution of these regions are needed for analysis in greater detail.

Below the Lorentzian/Gaussian boundary seen in Figure 4.3, there is a region containing a large number of yellow pixels corresponding to neither a Lorentzian nor Gaussian fit. This region contains spectra which tend to decorrelate very slowly and hence the ACFs show almost no change in power across the lags. In this case, fitting a Gaussian or Lorentzian curve to ACFs phase is has no meaning and that is why neither fit is best. If the region was looked at using a different frequency, the ACFs would most likely show a Gaussian fit due to the long decorrelation.

### **4.3 Phase transition in the high-latitude F-region plasma**

Previous SuperDARN radar observations have shown the spectral width boundary (the boundary between the low and high spectral widths) coincides with the nightside open-closed magnetic field line boundary (Parkinson et al., 2002). This is a significant result because it shows that SuperDARN radars can be used to monitor expansions and contractions of the polar cap ionosphere in response to changing solar wind and geomagnetic conditions. Parkinson et al. (2004), hypothesised that the formation of the spectral width boundary, as seen by TIGER, is influenced by a step-like increase in Pederson conductivity.

When comparing the boundary seen between the Lorentzian and Gaussian standard deviation zones to the spectral width plots in Figure 4.3, it can be seen that the areas where the Lorentzian standard deviation is lowest generally corresponds to areas of high spectral widths. Conversely, areas where the Gaussian standard deviation is lowest generally corresponds to areas of low spectral widths. However, this is not always necessarily so, as pointed out in section 4.2.

The result mentioned above implies that the ionospheric plasma on open magnetic field lines has a correlation length shorter than the scattering wavelength, whereas the ionospheric plasma on closed magnetic field lines exhibit correlation lengths larger than the scattering wavelength. This further shows that the ionospheric irregularities rapidly decorrelate in the turbulent high spectral width region, whereas they preserve their coherence over larger spatial scales in the more laminar low spectral width region of the auroral oval.

The boundary between the spectral widths corresponds to the open-closed field line boundary. Across this boundary, at ~1500km, not only do the spectral widths increase, but also the plasma changes in its correlation times and lengths. One other noticeable change in this region is the rapid increase in line of sight velocities in the poleward direction which correspond to flow bursts which commence on open field lines (Parkinson et al., 2004). These results all support a phase transition in the plasma characteristics across the open-closed magnetic field lines.

## Chapter 5 – Multi-peaked Doppler spectra

### 5.1 Identification of multi-peaked Doppler spectra

Numerous ACFs consistent with single-peaked Doppler spectra are observed using SuperDARN radars. These ACFs are analysed using the FITACF program to extract data about their properties. FITACF assumes a single-peaked spectrum when fitting to the ACF (as discussed in section 2.4); hence erroneous results can be obtained when the spectra are actually multi-peaked. The Doppler spectra calculated from the ACFs also have a limited Doppler resolution which explains why the normal technique does a poor job of resolving multi-peaked spectra.

Characteristics of the Doppler spectra corresponding to the SuperDARN ACFs are determined as follows. If we make an analogy between a time series and the ACFs, the sampling frequency of the time series is

$$f_s = \frac{1}{\tau} \quad (5.1)$$

where  $\tau$  is the fundamental lag length which is 2400  $\mu\text{s}$  for the standard SuperDARN pulse set. This then yields the Nyquist frequency via

$$f_N = \frac{\pm f_s}{2} \quad (5.2)$$

The Nyquist frequency determines the maximum frequency that can be reproduced without aliasing. In the case of SuperDARN radars,  $f_N \sim \pm 208$  Hz. Using the Doppler shift equation, the corresponding Nyquist velocity is

$$v_N = \frac{\pm f_N \lambda_0}{2} \quad (5.3)$$

where  $\lambda_0$  is wavelength of the radar. For a radar frequency of 12 MHz, the radar wavelength is  $\sim 25$  m. This gives a Nyquist velocity of 2594  $\text{m s}^{-1}$ , an estimate of the maximum line-of-sight velocity that can be measured by the radars.

The frequency resolution of the spectrum is given by the inverse of the effective time series length, in this case  $27\tau$ , the maximum number of lags in the ACF. Then using equation (5.3), the corresponding Doppler velocity resolution is  $96 \text{ m s}^{-1}$ . This Doppler resolution is rather crude for the detection of all but the most widely separated multi-peaked spectra.

To help resolve multi-peaked spectra, a new method of analysing the data was needed in the form of Burg analysis (Burg, 1975). This method of fitting a statistical regressive function to the data was employed to try to find if, and where these multi-peaked spectra occur (Danskin et al., 2004). The Burg analysis takes the original lags and estimates further lags in the sequence. The estimation principle used is that of the maximum entropy method — the spectral estimate must be the most random or have the most entropy of any power spectrum which is consistent with the measured data (Burg, 1975). The result of this new analysis technique is that it achieves better spectral resolution than obtained using Fourier transform (FFT) analysis. The first stage involved fitting a Burg function to all of the ACF lags for a chosen beam and set of ranges. As this process currently takes large computational time, we only analysed four hours of data recorded during 10 December 1999. Once the data had been analysed, a subset of the resulting Doppler spectra were compared with the corresponding Doppler spectra derived from the FFT of the ACF.

Another way of studying the multi-peaked spectra made use of summary plots. Every group range with a multi-peaked spectrum, as identified using the Burg analysis, was identified in a summary plot. This required the development of a new program to extract the characteristics of the spectra observed by the Burg method, whilst applying constraints to ensure mathematical ghosts were not displayed. The resulting summary plot could then be used to compare the behaviour of multi-peaked spectra with the behaviour of other familiar parameters, such as the power, line-of-sight velocity, and spectral width.

## 5.2 Doppler characteristics observed using the Burg analysis

Here we employ two ways of examining the data produced by Burg analysis. The first compared the Burg computed Doppler spectra with the Doppler spectra obtained from the Fourier transform of the ACFs.

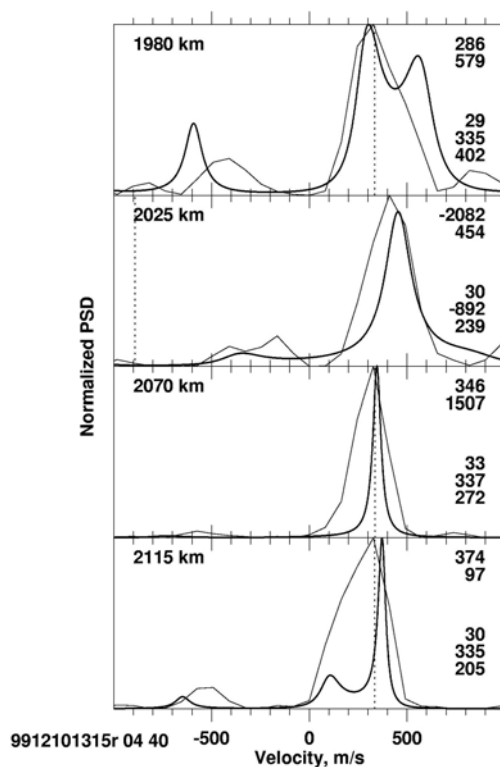


**Figure 5.1:** A comparison between Doppler spectra obtained using a Burg analysis (thick lines) and an FFT of the ACF data (thin lines) for TIGER beam 4 at 1315 UT on 10 December 1999.

As can be seen in Figure 5.1, the thin lines represent the Doppler spectra which are determined by FFTs of the ACFs. These do not appear smooth because of their previously calculated Doppler resolution of approximately  $96 \text{ m s}^{-1}$  hence the sharp changes in values for successive points. The thick lines represent the Burg method fits to the data, and they display continuous smooth lines which describe what is assumed to be happening across the entire spectral range. Due to the way the Burg analysis fits functions to the data, more detailed Doppler spectra are calculated with a better spectral resolution.

In Figure 5.1, there are spectra that would normally be identified as single peaked spectra, but now the Burg analysis clearly identifies them as multi-peaked spectra. For example, this is noticeable when looking at the broad spectral peak recorded at range 2115 km. Here, a single-peaked spectrum with a FITACF spectral width of  $205 \text{ m s}^{-1}$  is resolved into two peaks by the Burg analysis. The poor Doppler resolution obtained from the FFT of the ACF prevents resolution of this feature. This demonstrates how the Burg

analysis can be used to infer the existence of features, such as multiple peaks, that otherwise would not be resolved.

### **5.3 Occurrence of multi-peaked spectra**

The Doppler spectra created using the Burg analysis illustrated the presence of multi-peaked spectra where previously the FFT of the ACFs showed only single peaks. To further examine the occurrence of multi-peaked spectra with respect to geophysical boundaries, a summary plot of the occurrences of these spectra was needed. A new program “*multipeak.pro*” was created to analyse the *.txt* data created by the Burg analysis of the raw data files. Here we only considered characteristics of the first two major peaks because lesser peaks were more likely to be ghosts. The program *multipeak* extracted the data from the Burg *.txt* files. *Multipeak* then sorted the data according to parameters such as beam number, ground scatter and quality flags. One of the main objectives of the program was to remove suspect data points. A set of criteria was established to ensure the credibility of results. The criteria were, first, both major peaks must have power greater than 10 dB so as to avoid noise peaks. Second, the spectral width must be greater than zero so as to avoid unrealistic data points. Third, the difference in power between the two peaks must be no greater than 6 dB so that the second peak was not a sideband of the main peak. Finally the velocities of each peak must be less than the Nyquist velocity. The program stored the parameters characterising the filtered multi-peaked data in a new file which had the correct format for input to the summary plotter. This allowed the data pertaining to multi-peaked spectra to be viewed over extended intervals, and to be compared to other parameters such as power, line-of-sight Doppler velocity, and spectral width.

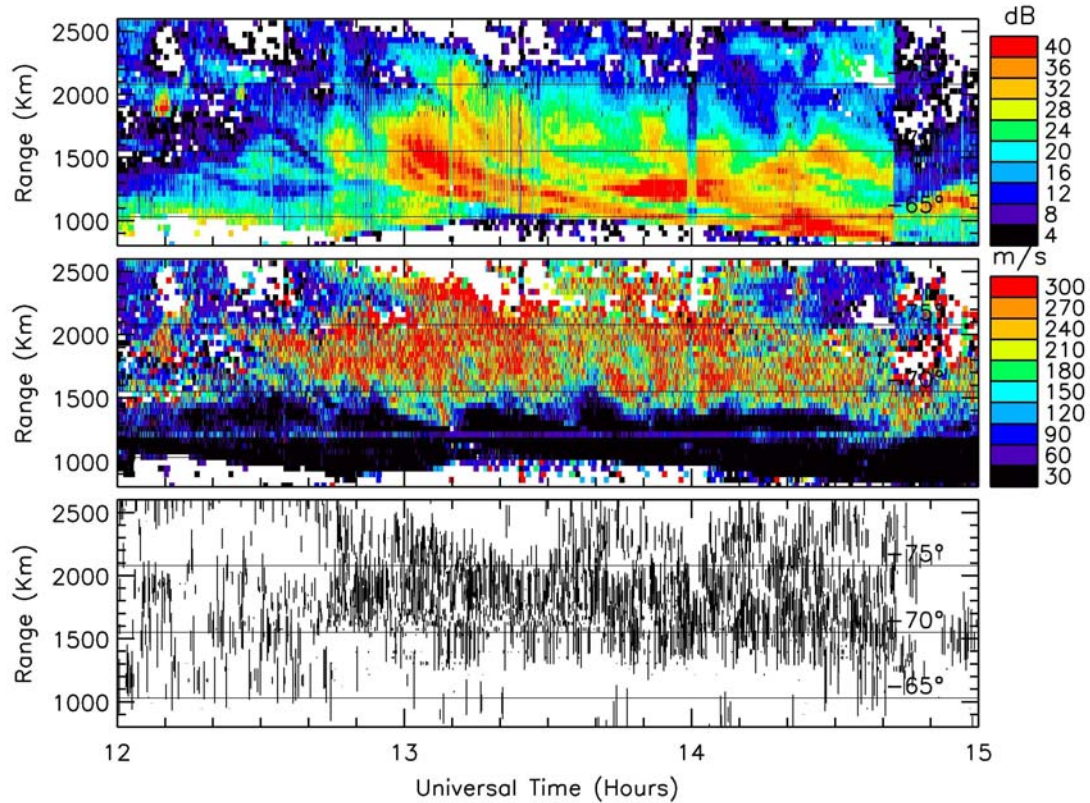


**Figure 5.2:** Summary plot of TIGER beam 4 observations during 1200 to 1500 UT on 10 December 1999 with the backscatter power (dB) (top panel), Lorentzian spectral width ( $\text{m s}^{-1}$ ) (middle panel), and occurrence of multi-peaked spectra (bottom panel) are shown. In the bottom panel, the length of the lines represent the velocity difference between the two major peaks.

Figure 5.2 compares the occurrence of multi-peaked spectra with other radar parameters. There is no obvious association between the backscattered power and the occurrence of multi-peaked spectra, other than that determined by the 10-dB threshold. However, there is an association between the occurrence of the spectral widths and the multi-peaked spectra. Whilst there are isolated regions where the multi-peaked spectra coincide with low spectral widths, to first order the multi-peaked spectra coincide with the regions of high spectral width. This result is not totally unexpected because regions of high spectral width are more likely to correspond to regions of small-scale electric field fluctuations (Huber and Sofko, 2000).

In their original study of E-region scatter, Danskin et al. (2004) suggested a cause of the multi-peaked spectra was the simultaneous detection of echoes from the top and bottom of the electrojet layer. Here the Burg analysis has been applied to the F region scatter for

the first time, and we suggest that multi-peaked spectra occur because of small-scale vortices associated with filamentary field-aligned currents (Huber and Sofko, 2000). Consistent with the results found in the previous chapter, the occurrence of multi-peaked spectra in the high spectral width region shows that the plasma is more turbulent in this region.

## Summary and Conclusions

TIGER SuperDARN HF radar data can be used to identify plasma characteristics in the sub-auroral, auroral, and polar cap ionosphere. This study investigated various characteristics of the plasma that change across the spectral width boundary (SWB). Previous studies (Lester et al., 2001; Parkinson et al., 2002; Chisham et al., 2003) have shown that the spectral width boundary coincides with the open-closed magnetic field line boundary (OCB) in the pre-midnight sector. As the OCB is a constantly fluctuating region that is ever shifting due to changes in solar wind and magnetic storm conditions, it is an important to develop techniques to identify and monitor its complex behaviour.

To start this study, the Doppler characteristics of the deep polar cap ionosphere were investigated. Using both the Halley and TIGER HF radars, it was seen that the dominant source of movement was, as expected, due to antisunward drift. This drift exhibited larger velocities and spectral widths in the dayside polar cap imaged by the Halley radar. The velocities and spectral widths decayed throughout the nightside polar cap imaged by the TIGER radar. In a sense, a spectral width boundary existed in the deep polar cap, and it did not necessarily correspond to the OCB. This has direct implications for the plasma characteristics of the separate day and night side regions. As the fields of view for both the Halley and TIGER radars do not overlap, there is a region within the deep polar cap that was not viewed. This observational void will be filled when the PolarDARN radars are deployed.

When looking at the SWB, the characteristics of the Doppler spectra change from narrow peaked spectra equatorward of the boundary to broad peaked spectra poleward of the boundary. The spectral width is determined by how rapidly the ACFs decay. For each ACF, a curve is fitted to the data which represents the properties of the corresponding spectra. In the case of ionospheric scatter, Lorentzian and Gaussian curves, or a combination of both, best fit the ACFs. TIGER observations were evaluated to determine a relationship between these fits and the SWB, and summary plots clearly revealed spatial organisation of the results. Unlike the earlier results of Hanuise et al. (1993) and Villain

et al. (1996), we found a close match between the SWB and the spectral type. Lorentzian Doppler spectra tended to occur in the large spectral width region poleward of the SWB, whereas Gaussian Doppler spectra tended to occur in the low spectral width region equatorward of the SWB. This confirms the existence of a phase transition in the plasma characteristics across this boundary.

The Doppler spectra obtained with SuperDARN radars are calculated from the fast Fourier transform (FFT) of the autocorrelation functions (ACFs) of the backscattered signal. The standard SuperDARN analysis techniques known as FITACF assumes the Doppler spectra are single-peaked. Due to the poor Doppler resolution obtained from the FFT of the ACFs, multiple peaks tend to merge into single peaks within these spectra. A new form of analysis known as Burg analysis was applied to the data to improve the interpretation of the ACF data. The Burg analysis improved the Doppler velocity resolution and revealed many multi-peaked spectra concentrated in the large spectral width zones. This result is not totally unexpected because regions of high spectral width are more likely to correspond to regions of small-scale electric field fluctuations (Huber and Sofko, 2000). This is consistent with present theories and shows that the plasma is more turbulent in this region.

This study has shown changes in the spectral widths, Doppler velocities, Doppler spectra type (Gaussian vs. Lorentzian), and the occurrence of multi-peaked spectra across the open-closed magnetic field line boundary. Again, this confirms the existence of a phase transition in the plasma characteristics across this boundary.

## References

- Anderson, D. N., J. Buchau, et al. (1988). *Origin of density enhancements in the winter polar-cap ionosphere*. *Radio Science* **18**: 513-519.
- Baker, K. B. FITACF - A SuperDARN Tutorial.
- Baker, K. B., R. A. Greenwald, et al. (1989). *PACE, Polar Anglo-American Conjugate experiment*. *Eos* **22**: 785-799.
- Baker, K. B., J. R. Dudeney, et al. (1995). *HF radar signatures of the cusp and low-latitude boundary layer*. *Journal of Geophysical Research* **100**: 7671-7695.
- Balthazor, R. *The Space and Atmosphere Research Group*,  
<http://www.shef.ac.uk/~sparc/tutorial.html> Date accessed: 22/9/04
- Barnes, R. *SuperDARN*, <http://superdarn.jhuapl.edu/> Date accessed: 10/03/04
- Burg, J. P. (1975). Maximum entropy spectral analysis. Department of Geophysics, Stanford University.
- CALSPACE Lockheed/UC Berkeley Centre of Excellence - Aurora Forecast,  
<http://sprg.ssl.berkeley.edu/forecast/welcome.html> Date accessed: 05/07/04
- Chen, F. F. (1984). *Introduction to plasma physics and controlled fusion*. New York, :Plenum Press.
- Chisham, G., M. P. Freeman, et al. (2003). *The SuperDARN spectral width boundary and how it relates to the open-closed field line boundary*. RAS/MIST discussion meeting, 10th October 2003, Society of Antiquaries Lecture Theatre, Burlington House, Piccadilly, London.
- Danskin, D. W., A. V. Koustov, et al. (2004). *Observations of double-peaked E region coherent spectra with the CUTLASS Finland HF radar*. *Radio Science* **39**.
- Dyson, P. L. and J. C. Devlin (2000). *The TIGER Radar - An Extension of SuperDARN to sub-auroral latitudes*. Workshop on Applications of Radio Science (WARS), La Trobe University, Beechworth Campus.
- Dyson, P. L., J. C. Devlin, et al. (2003). *The Tasman international geospace environment radar (TIGER) - current development and future plans*. Radar Conference, 2003. Proceedings of the International.

- Greenwald, R. A., K. B. Baker, et al. (1985). *An HF phased array radar for studying small-scale structure in the high-latitude ionosphere*. *Radio Science* **20**: 63-74.
- Greenwald, R. A., K. B. Baker, et al. (1995). *DARN/SuperDARN: A global view of the dynamics of high latitude convection*. *Space Science Review* **71**: 761-796.
- Gresillon, D., B. Cabrit, et al. (1992). *Collective scattering of electromagnetic waves and the cross-B plasma diffusion*. *Plasma Physics and Controlled Fusion* **34**: 1985-1991.
- Hackworth, M. <http://www.physics.isu.edu/weather/> Date accessed: 02/10/04
- Hanuse, C., J.-P. Villain, et al. (1993). *Interpretation of HF radar ionospheric Doppler spectra by collective wave scattering theory*. *Annales Geophysicae* **11**: 29-39.
- Hargreaves, J. K. (1979). *The upper atmosphere and solar-terrestrial relations : an introduction to the aerospace environment*. New York, Van Nostrand Reinhold.
- Hargreaves, J. K. (1992). *The solar-terrestrial environment : an introduction to geospace-the science of the terrestrial upper atmosphere, ionosphere, and magnetosphere*. Cambridge [England] ; New York, NY, USA, Cambridge University Press.
- Huber, M. and G. J. Sofko (2000). *Small-scale vortices in the high-latitude F region*. *Journal of Geophysical Research* **105**: 20885-20897.
- Hunsucker, R. D. and J. K. Hargreaves (2002). *The high-latitude ionosphere and its effects on radio propagation*. Cambridge New York, Cambridge University Press.
- Lester, M., S. Milan, et al. (1998). *CUTLASS Tutorial*. CUTLASS Workshop, University of Leicester, 2nd - 3rd December, 1998.
- Lester, M., S. E. Milan, et al. (2001). *A case study of HF radar spectra and 630.0 nm auroral emission in the pre-midnight sector*. *Annales Geophysicae* **19**: 327-339.
- Mathews, J. D., J. Doherty, et al. (2002). *An update on UHF radar meteor observations and associated signal processing techniques at Arecibo Observatory*. *Journal of Atmospheric and Solar-Terrestrial Physics* **65**: 1139-1149.
- Parkinson, M. L., P. L. Dyson, et al. (2002). *Signatures of the midnight open-closed magnetic field line boundaries during balanced dayside and nightside reconnection*. *Annales Geophysicae* **20**: 1617-1630.

- Parkinson, M. L., G. Chisham, et al. (2004). *Magnetic local time, substorm, and particle precipitation-related variations in the behaviour of SuperDARN Doppler spectral widths*. *Annales Geophysicae*.
- Rishbeth, H. and O. K. Garriot (1969). *Introduction to ionospheric physics*. New York, Academic Press.
- Scolvi, G. (1970). *The Polar Ionosphere and Magnetospheric Processes*, Gordon and Breach, New York.
- Spaceweb <http://www oulu.fi/~spaceweb/textbook/> Date accessed: 12/08/04
- UASD *SHARE* radar, Halley, <http://www.nerc-bas.ac.uk/public/uasd/instrums/share/intro.html> Date accessed: 15/9/04
- Villain, J.-P., R. Andre, et al. (1996). *Observation of the high latitude ionosphere by HF radars: interpretation in terms of collective wave scattering and characterization of turbulence*. *Journal of Atmospheric and Terrestrial Physics* **58**: 943-958.
- Whitehead, J. D. (1971). *Difficulty Associated with Wind-Shear Theory of Sporadic E*,. *Journal of Geophysical Research* **76**: 3127-3135.